

November 10, 2005
Physical Biosciences Division
Lawrence Berkeley National Laboratory
1 Cyclotron Road, M.S. 977-152
Berkeley, CA 94720

Yves Brun
Systems Biology/ Microbiology Faculty Search
Dept. of Biology
Indiana University
Jordan Hall 142, 1001 E. 3rd St.
Bloomington, IN 47405-7005

Dear Dr. Brun,

I am applying for a position of Assistant Professor for one of your openings in systems biology and microbiology, in response to an advertisement that was posted in *Nature*.

I am a postdoctoral fellow in the Physical Biosciences Division of Lawrence Berkeley National Laboratory, where I am pursuing research in systems biology in Adam Arkin and Jay Groves's laboratories. I received my doctorate at Stanford University in the Department of Chemistry under the supervision of Professor Steven Boxer and then did a short post-doc in systems biology at the University of Cambridge with Dr. Dennis Bray.

Enclosed are: an application packet, which includes my curriculum vitae, a statement of research plans, and a statement of teaching interests, and copies of three recent publications. My four most recent and current advisors have sent recommendations to your address. For more information about me, including pdf's of all my publications and copies of the software that I have written, please see my web page: <http://sahara.lbl.gov/~sandrews/index.html>.

My research combines analytical theory, computational work, and *in vitro* and *in vivo* experiments to investigate a particularly intriguing biochemical network that is a component of the *E. coli* cell division cycle, called the Min system. I plan to continue this work over the next several years and also broaden the scope to explore other portions of the cell division cycle. I believe that these topics would be well suited to your department because they combine cutting-edge theoretical and experimental approaches to quantitatively investigate fundamental problems in physical biology.

Thank you for considering my application. Please let me know if you have any questions.

Sincerely,



Steven S. Andrews



Cell Division in Prokaryotes: Physical Chemistry in a Biological Environment

Overview	2
Summary of Research Accomplishments	2
Undergraduate and pre-doctoral research	2
Doctoral research	2
Post-doctoral research	3
Systems Biology of Prokaryotic Cell Division	6
Research Plans	9
Theoretical investigations of cell division	9
Experimental research – <i>in vitro</i> experiments	10
Experimental research – <i>in vivo</i> experiments	12
Summary	13
Literature Cited	14
Teaching Experience and Interests	18
<i>Curriculum Vitae</i>	19
References	23

Contact: Steven S. Andrews
Lawrence Berkeley National Laboratory
1 Cyclotron Road, M.S. 977-152
Berkeley, CA 94720
Phone: 510-710-9989
Fax: 510-486-6219
E-mail: ssandrews@lbl.gov
Website: <http://sahara.lbl.gov/~sandrews/index.html>

Overview

My research will investigate the network of chemical and physical processes that are combined in the prokaryotic cell division cycle. These processes are remarkably rich, involving spatial organization of cells, bacterial decision-making about when to divide and about where the division plane should be, and the mechanical processes of annulus formation and contraction.

This project is at the core of fundamental biology since it connects inanimate physical processes to biological reproduction. However, it is not just academic. Bacteria comprise roughly 50% of the Earth's biomass¹, cause about 10% of human deaths, play a major role in the global climate, and degrade a large fraction of our pollution. Improved knowledge of bacterial cell division will provide targets for better antibiotics and will allow us to engineer bacteria in ways that help society. Also, prokaryotes are often excellent models for eukaryotes. Discoveries with these simpler prokaryotes are likely to speed up discoveries for eukaryotes, eventually leading to better health care and sustainable agriculture.

My initial work will be on the *Escherichia coli* Min system, which is involved in determining the site for cell division. It is comprised of only the proteins MinC, MinD, and MinE and yet it exhibits intriguing oscillations in which a polymer filament is alternately assembled and disassembled at opposite ends of the cell. The methods of my research will include computational modeling, *in vitro* and *in vivo* microscopy, and experimental physical chemistry. As we develop a better understanding of the *E. coli* Min system, I plan to expand the scope of my research to explore more of the *E. coli* cell division cycle. I also plan to investigate cell division in other bacteria, partly to allow comparisons with *E. coli*, and partly to examine behaviors that *E. coli* do not exhibit, such as sporulation. A tremendous amount remains to be discovered in prokaryotic cell division so it is nearly certain that we will stumble upon completely unexpected phenomena; these, of course, will help guide the research direction as well.

Summary of Research Accomplishments

Undergraduate and pre-doctoral research

As an undergraduate at Dartmouth College, I studied the statistical mechanics of polymer melts², quantified the degree to which polymers that fold in constricted spaces naturally form α -helices and β -sheets, and derived the properties of a worm-like chain³. These were excellent training for my current work on membrane-bound protein polymers⁴. After college, I showed that ultraviolet solar irradiation is a dominant influence in the marine carbon cycle^{5,6}: it breaks down organic carbon from terrestrial sources, which cannot be used by most marine life, into forms that are biologically labile.

Doctoral research

In Steven Boxer's laboratory, I studied the effects of electric fields on molecular vibrations, called vibrational Stark effects⁷. These are exceedingly small: a 5000 kilovolt per centimeter electric field, which is the largest field that can be reliably applied to a condensed phase sample,

changes both vibrational frequencies and infrared absorption intensities by less than one part in 10^4 for most molecules^{8,9}. No one had quantified vibrational Stark effects before, so I designed the necessary instrumentation¹⁰, electronics¹¹, and data analysis software¹². Using these, Eunice Park and I showed that vibrational Stark effects can be used to directly measure electric fields on very small scales, including *inside* proteins. Using a carbon monoxide molecule as the world's smallest electric field sensor, we determined that the electric field inside a myoglobin protein changes by 8 MV/cm when histidine-64 is protonated⁹ (figure 1). Several graduate students have worked, and are working, on research that lead directly from my initial explorations¹³⁻¹⁵. I also derived the quantum mechanical theory of vibrational Stark effects¹⁶: for nitriles, frequency changes arise from nearly equal contributions of mechanical anharmonicity of chemical bonds and electronic perturbations of the bond strengths.

With the same methods, I measured the effect of an electric field on a mixed-valence electronic transition of the bacterial photosynthetic reaction center¹⁷, which was the first measurement of its kind. It was used to show that the radical electron is delocalized over two bacteriochlorophylls and that there is significant coupling between this and other transitions.

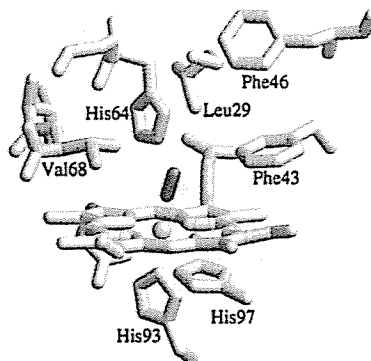


Figure 1. Diagram of carbon monoxide (center rod-shaped molecule) bound to the heme iron in myoglobin and nearby amino acids⁹. The frequency of the carbon monoxide stretching vibration is affected by the local electric field, which is strongly influenced by charged atoms on nearby residues. Detection with infrared spectroscopy and calibration with externally applied electric fields allowed us to quantify the internal electric fields that are produced by pH changes or mutations.

Post-doctoral research

I switched research fields from chemical physics to systems biology, so I chose to take two post-doctoral positions to gain a broader range of experiences. The first was at the University of Cambridge with Dennis Bray and the other at the Lawrence Berkeley National Laboratory with Adam Arkin. This may not have been a wise career choice because I devoted a relatively large amount of time to identifying interesting projects and to learning about the research topics in each laboratory and not enough to creating new research results. Nevertheless, I believe that these experiences will prove to be beneficial in the long run.

My initial project was to develop a computational model of the *E. coli* chemotaxis signaling network that accounted for both three-dimensional space and single molecules, which was an extension of current laboratory work¹⁸. However, neither software programs nor computer

algorithms existed that could accurately and efficiently simulate chemical reactions between individual molecules in solution. Thus, I designed the necessary algorithms (figure 2) and incorporated them in a general purpose program called *Smoldyn*¹⁹ (short for *Smoluchowski dynamics*). Results have been popular: during 2004, the number of downloads of my publication that describes the algorithm²⁰ was in the top 10% of those for all articles published by the Institute of Physics and in the top 10 of articles published by *Physical Biology*; *Smoldyn* is used in several laboratories in the U.S.²¹, Britain, India, Japan, and the Netherlands; *Smoldyn* was a focus of two summer classes taught at the Marine Biological Laboratories; and my algorithms are being implemented in *ChemCell*, which is a simulation tool in development at Sandia National Laboratory²².

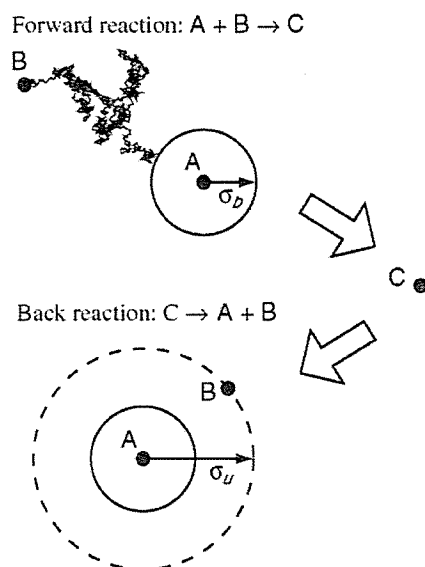


Figure 2. Algorithm for simulating forward and back bimolecular reactions used in *Smoldyn*, shown in the reference frame of an 'A' molecule²⁰. A forward reaction occurs when the centers of an A and a B molecule (black dots) diffuse to a separation that is equal to the binding radius, σ_b (circle with solid line), forming a C molecule. When a back reaction occurs, the A and B products are initially separated by the unbinding radius, σ_u (circle with dashed line), which is made larger than the binding radius so as to prevent the instant recombination of the products. For computational efficiency, diffusion is simulated with relatively long steps and the sizes of the binding and unbinding radii are modified to yield quantitatively accurate reaction rates.

The computational model of *E. coli* chemotaxis was completed in collaboration with Karen Lipkow (figure 3). We found that diffusion produces a significant signaling delay between the chemotaxis receptors and the flagellar motors and that it varies for different motors^{23,24}; the nucleoid or large protein complexes provide obstructions that enhance these effects. I also investigated the serial rebindings of a single ligand molecule to a cluster of receptors²⁵. Receptor clustering does not affect the overall level of the signal that is received, but instead leads to temporally and spatially correlated binding events. This increases the signaling noise which may allow a signal to be sensed above background noise.

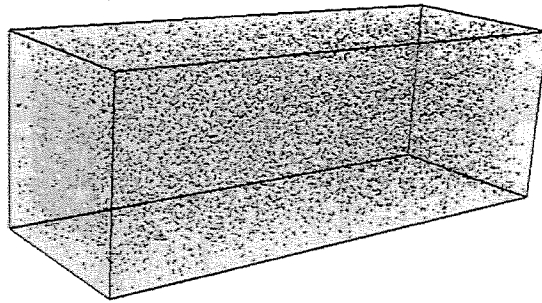


Figure 3. Sample output from the Smoldyn program showing individual chemotaxis proteins in an *E. coli* cell²⁵. Color codes: gray, inactive CheA; orange, active CheA; yellow, phosphorylated CheA; green, CheZ; dark brown, CheY; red, CheYp; blue, FliM; cyan, FliM-CheYp. The cell is shown 0.1 s after addition of a saturating repellent stimulus. Not shown are obstructions to diffusion, which were shown to have a significant effect on signaling delays.

Next, I decided to investigate the evolution of biochemical reaction networks. Simulated bacteria were defined with various metabolic networks which obeyed all physical laws. They competed and evolved in a simulated chemostat. I found that different environments favored different metabolic networks: low chemostat dilution rates caused evolution towards small metabolic networks, multiple co-existing bacterial strains, and strategies that favored specialization on a single substrate; high dilution rates produced opposite effects^{26,27}. In the former case, only those individuals that used all available resources were able to grow fast enough to avoid being washed out of the chemostat; in the latter, the low resource availability meant that a metabolic cost that was imposed on generalists became unaffordable.

While fascinating, the evolution research was a departure from my interests in physical biology, so I refocused on the *E. coli* Min system (figure 4) and built the foundation of the work that I'm planning for the next several years. My initial computational models²⁸ highlighted key aspects of the system that were not understood: *i.* what determines the shape of the MinD polymer? *ii.* why is there one MinD polymer rather than many? and *iii.* what are the MinD polymerization rates and dynamics? In addressing the first question, I suspected that the helical shape arises because it is the lowest energy conformation of a stiff polymer that is bound to a rod-shaped membrane. To investigate this, I derived a theory of polymer shapes on curved surfaces⁴ and found that not only does this hypothesis explain the MinD shape, but it can also explain the shapes of several other cytoskeletal polymers (figure 5). Furthermore, it provides a simple explanation for remarkable dynamics that are observed with the septum-determining Z-ring in sporulating *B. subtilis*²⁹: a ring forms at the mid-cell, transforms to a helix, transforms again into two polar rings, and finally a polar ring constricts to separate the mother cell from the spore. Minor changes in the Z-ring composition are sufficient to produce these dynamics.

To investigate the third question posed above, I needed biology laboratory experience. So, I took the Cold Springs Harbor Laboratory summer course in Advanced Bacterial Genetics, formed collaborations with the Rothfield and King labs (both at the University of Connecticut Health Center), and changed my post-doc appointment such that I am now co-advised by both Adam Arkin and Jay Groves. In collaboration with Jeff Nye, we are working to image fluorophore-labeled MinD polymer filaments on *in vitro* bilayers. This work is described below.

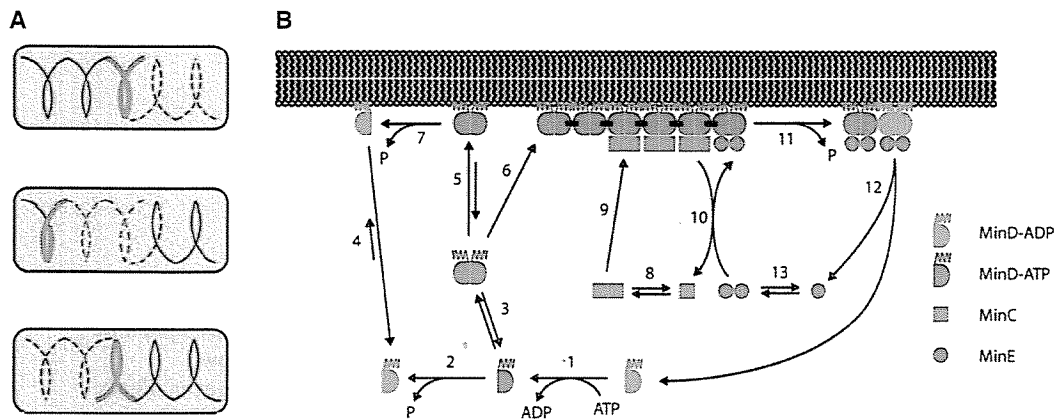


Figure 4. A. Dynamics of the Min system (figure is from Gitai and Shapiro³⁰). MinD (blue lines) forms a helical polymer that extends the length of the bacterium but is primarily at one cell pole. MinE (red) binds to MinD and disassembles the polymer with migration towards a cell pole. The MinD polymer reassembles at the far pole, leading to more disassembly by MinE. The system oscillates with a period of about 40 seconds. B. A nearly complete set of reactions in the Min system, assembled from the literature. 1. Transfer of nucleotide bound to MinD^{31,32}. 2. Hydrolysis of ATP by cytoplasmic MinD^{31,33,34}. 3. Dimerization of MinD³⁵⁻³⁷. 4. Interaction of MinD-ADP with membrane³⁸. 5. Binding of MinD dimer to membrane with amphipathic helices of both monomers^{34,35,37-40}. 6. Polymerization of MinD on the membrane^{35,41,42}. 7. Hydrolysis of ATP by unactivated membrane-bound MinD^{33,34,37,39}. 8. Dimerization of MinC⁴³⁻⁴⁵. 9. Binding of MinC to membrane-bound MinD^{37,44}. 10. Displacement of MinC by MinE^{36,46}. 11. Hydrolysis of ATP by MinD, activated by MinE, leading to depolymerization and, possibly, retraction of the lipid-binding helices^{33,34,37,39}. 12. Release of MinE from MinD and MinD from the membrane^{34,35,42}. 13. Dimerization of MinE⁴⁷.

Systems Biology of Prokaryotic Cell Division

Prokaryotic cell division involves several linked components⁴⁸: *i.* replication and segregation of the chromosome, *ii.* segregation of any plasmids into the two halves of the cell, *iii.* placement and assembly of a central protein ring, called the Z-ring, and *iv.* contraction of the Z-ring, followed by re-arrangement of the cell walls at the new poles.

As the chromosome is replicated, the origin regions move rapidly apart, but only migrate part of the way towards opposite cell poles. An exception includes sporulating *B. subtilis*, in which the chromosomes move to the extreme poles. It is likely that the chromosomes are actively moved along an intra-cellular helical track comprised of the actin-analog MreB^{49,50}. The components that attach the chromosome to the MreB cables remain unknown, as do the mechanisms that provide motion.

Plasmids appear to replicate randomly over time, although their segregation is still highly orchestrated. Low-copy-number plasmids include the ParA and ParB proteins and are moved from the mid-cell position to the quarter-cell positions, or they include ParM and ParR and are

localized near the cell poles⁵¹. In the former case, ParA forms a helical filament on the surface of the nucleoid which, somehow, pushes the plasmids to the correct locations⁵². ParM forms a double stranded polymer filament that is capped on both ends by ParR⁵³; ParR is bound to the plasmids, so extension of ParM through polymerization pushes the plasmids apart and towards the cell poles. High-copy number plasmids do not encode partitioning systems but form isolated plasmids and clusters that move around the cell with unknown mechanisms⁵¹.

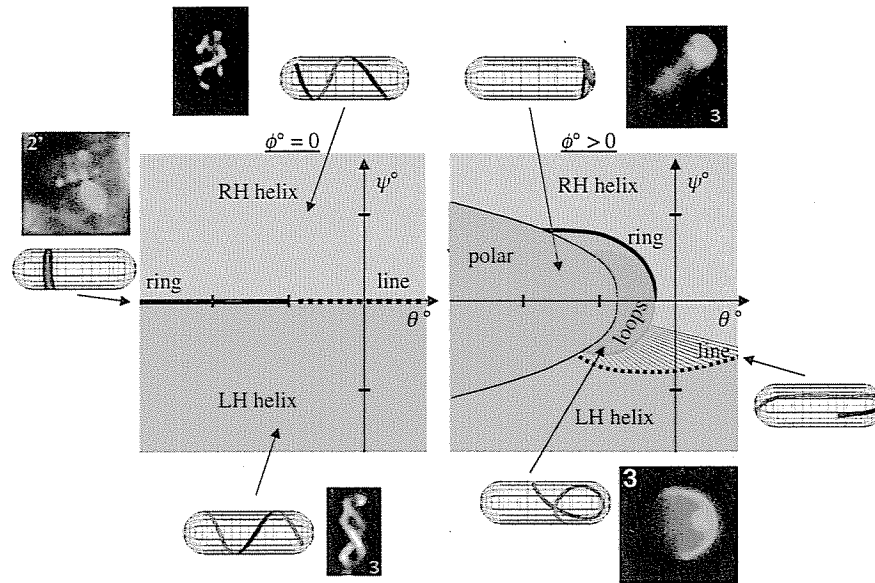


Figure 5. Diagrams of how monomer shape parameters affect the conformations of polymers that are bound to cell membranes. Monomer shapes are defined by yaw (ϕ° , two panels), pitch (θ° , horizontal axis), and roll (ψ° , vertical axis). Resulting polymer morphologies are: rings (heavy line; image shows FtsZ⁵²), right-handed helices (green region; image shows Mbl⁵⁵), left-handed helices (red region; image shows MreB⁴¹), lines (dashed line; no biological example known), polar-targeted polymers (orange region; image shows MinD⁴¹), and loops (green region; image shows MinD on a spherical cell⁵⁶). Illustrations of polymers on a rod-shape were generated by a computational model for the theory that I developed on this topic. The phase diagram for $\phi^\circ > 0$ is not exact but estimated; the light black lines shown here are a feature of Microsoft Word and not of the model. Each tick mark on the axes represents a bending angle of $L/2R$, where L is the length of a monomer and R is the radius of the bacterium.

Concurrent with DNA segregation, the Z-ring is assembled around the cell center, mostly from mostly the tubulin-analog FtsZ⁵⁷. It is placed at mid-cell by a combination of two negative regulatory systems. In nucleoid occlusion, Z-ring formation is inhibited around either of the two daughter chromosomes^{58,59}. The Min system, mentioned above, provides a static inhibition near the poles in *B. subtilis*⁶⁰ and a remarkable dynamic inhibition in *E. coli*³⁰ (figure 4). Here, MinD polymerizes on the inside of the cell membrane as a helical filament that extends from one pole of the cell towards the other⁴¹. It is then disassembled by MinE, reforms at the opposite pole, is disassembled, and so on, with a roughly 40 second oscillation period. FtsZ polymerization is inhibited by MinC, which binds to and colocalizes with MinD. MinC is rarely at the mid-cell because of the MinD/MinE oscillation, thus allowing Z-ring formation only at the mid-cell.

Finally, the Z-ring constricts to divide the cell in half. The control system that regulates the timing of division for *E. coli* and *B. subtilis* is unknown⁴⁸, as is the mechanism of Z-ring constriction^{57,61}. As mentioned above though, my theory on polymer conformations suggests that constriction could occur through a minor change in the Z-ring composition.

It is interesting to note that nearly every process in the prokaryotic cell division cycle is highly spatially organized, involves rapid dynamics, and relies on polymerized protein filaments. Also, few of these processes occur in either the cytoplasm or a membrane alone, but, instead, they involve constant exchanges between the cytoplasm and membrane. Finally, some of the proteins (MreB⁵⁵, FtsZ⁶², and possibly others) are involved both in cell division and in determining the cell shape.

Research Plans

My research will build a detailed understanding of the *E. coli* Min system, followed by a detailed understanding of prokaryotic cell division. This is an exploration into how one of the most fundamental aspects of life arises from a network of inanimate physical processes. The focus is on prokaryotic cell division but the tools that we will develop will be broadly useful. My computational methods are able to simulate biochemical networks at a much higher level of detail than had been available before. In the laboratory, I will image the dynamics of protein polymers that are bound to supported lipid bilayers, which combines the precision of *in vitro* experiments with the natural interactions between protein and membrane; these experiments are completely new as well. Together, these methods will help open a new field of systems biology in which complex biological processes are examined with a greater degree of detail and rigor than are currently available.

Theoretical investigations of cell division

I plan to create a detailed computational model of the *E. coli* Min system. This is essential because the creation of the model will guide attention towards the critical components, the model will make predictions that will direct experiments, and a quantitative computational model is the only way to thoroughly verify a conceptual picture. Current computational models of the Min system⁶³⁻⁶⁸ are inadequate because none simulate three-dimensional diffusion, polymerization, and the set of experimentally verified reactions. Instead, they choose a sub-set of these processes with the result that each agrees with only certain aspects of experiments. For example, the model by Huang, Meir, and Wingreen⁶³ treats membrane-localized MinD using continuously variable concentrations. The model does an excellent job of demonstrating how oscillations can arise in such a system, but the fact is that the MinD polymer terminus either is or is not at a certain point, and cannot be meaningfully described by a concentration. As a result, their model does not capture polymerization of MinD. Perhaps because of the same approximations, the model does not display oscillations unless several model reaction rate constants and protein concentrations differ by more than an order of magnitude from experimental values.

The detailed model that I am building treats each protein individually, thus capturing polymerization dynamics with physical accuracy, as well as capturing stochasticity and correlations between reactions. The following simulation capabilities are needed: *i.* diffusion of individual molecules in the cytoplasm and on the membrane, *ii.* reactions between individual molecules in the cytoplasm, *iii.* polymerization reactions on the inner membrane surface, and *iv.* polymer relaxation and thermal motion on the membrane. I have derived the theory for and written most of these modules^{4,20,28}, although more work is needed for diffusion and reactions on membranes. Using similar methods as the ones that I developed for simulating reactions in 3-dimensional space, I plan to develop the theory and methods for accurately simulating bimolecular reactions on a membrane. Once completed, these modules will be linked together.

It appears that all of the protein polymers involved in cell division polymerize cooperatively^{53,61,69}, meaning that the polymerization rate is slower for very short polymers than for longer ones. Signs of cooperative polymerization include: there is a minimum concentration

of monomers for polymerization to occur, polymers are multi-stranded, and there are relatively few short polymers. MinD shows all of these signs: it does not polymerize when its concentration is below 2 to 3 μM ³⁵, MinD forms filament bundles *in vitro*⁴², and only a single MinD polymer is observed in each cell⁴¹. Most theoretical studies on cooperative polymerization are for the solution phase and ignore stochastic influences^{70,71}. I plan to revisit this topic using a microscopic physical description to improve our understanding of MinD and other cell-division polymers. A solution to this problem will solve the question posed above of why only a single MinD polymer is observed, and will enable our simulations to match reality in this respect.

Macromolecular crowding may be essential for the Min system to work. It is known to have a large effect on diffusion^{23,72,73}, it can speed up bimolecular reactions by an order of magnitude or more^{74,75}, and it channels metabolites⁷⁶. Using *Smoldyn* and other detailed simulation tools, I plan to investigate its role in the Min system and, more generally, in polymerization at cell membranes.

The same simulation tools that I am developing for the Min system can be used for a wide variety of other systems. As time permits, I plan to use them to model Z-ring dynamics, plasmid partitioning, chromosome segregation, and cell division processes in other species. My ultimate goal is to quantitatively simulate cell division from start to finish, for both wild-type and mutant cells. This landmark accomplishment would signify that cell division is reasonably well understood.

Experimental research – *in vitro* experiments

Quantitative results for the *E. coli* Min system, as with all the other cell division reaction networks, are best determined using *in vitro* experiments. Here, the experimental system is fully characterized and is easy to manipulate. It is simple to vary protein concentrations at will, use inorganic fluorescent probes that are relatively stable to photobleaching, and to choose various experimental geometries.

Based on my experience of modeling the Min system, it appears that the dynamics of MinD polymerization are particularly complex, and particularly poorly understood. How many strands wide is the polymer? Are new proteins added to the polymer as monomers, dimers, or larger oligomers? Are new proteins added directly from the cytoplasm, or do they bind to the membrane first and then diffuse along the membrane? Do polymers display interesting assembly or disassembly dynamics? What happens when one membrane-bound polymer crosses another? None of these answers are known for MinD, and few are known for any of the other cell-division polymers. I plan to answer these questions for MinD initially and, afterwards, for other cell-division polymers. This knowledge will enable modeling and, more importantly, will bring us closer to our goal of understanding cell division.

Recent developments in fluorescence microscopy have made this an extremely powerful tool, as well as the best current method for investigating polymerization dynamics⁷⁷. A veritable alphabet soup of new techniques include: FRAP (fluorescence recovery after photobleaching), FRET (fluorescence resonance energy transfer), TIRF (total internal reflection fluorescence microscopy), FCS (fluorescence correlation spectroscopy), and FLIM (fluorescence lifetime imaging microscopy). These powerful methods are relatively straight-forward to use.

To start to address the questions on MinD polymerization, I am working with a student named Jeff Nye to image MinD polymers on lipid bilayers, as mentioned above. The basis of our experimental system is a lipid bilayer that is supported on a glass substrate⁷⁸. The lipids are synthetic, which provides a much better defined system than is available with biological extracts. It also allows us to choose the bilayer composition, which is important because it was observed that MinD binds more tightly to anionic lipids than to neutral ones⁷⁹. There is a roughly 1 nm thick film of water between the glass substrate and the bilayer which makes both leaflets of the bilayer fluid and makes the bilayer mechanically similar to biological ones. Two percent of the lipids in the bilayer include a fluorescent probe, which does not appear to affect function, but allows the bilayer to be imaged and visually assessed for quality. Once the bilayer is formed, we add purified fluorescently-labeled MinD protein which polymerizes on the bilayer and is then imaged with an inverted microscope. I plan to use this method extensively during the next several years.

Relatively simple techniques with polymer imaging can reveal remarkable details about the polymerization process. The simple steady-state distribution of lengths of MinD polymers can be used to quantify the rate at which two filaments bind together, end-to-end, in a process called annealing⁸⁰. The assembly and disassembly rates of these filaments yield information about polymerization rates and binding constants⁷⁷. Combined with concentration-dependent information, they can also be analyzed to determine whether polymer growth occurs by monomer, dimer, or larger oligomer addition⁸¹. We may see dynamic instability, in which a polymer stochastically switches between either an elongation mode or a rapid disassembly mode⁵³. By using a mixture of fluorescently labeled and unlabeled MinD proteins, we expect to observe speckled polymers. The speckling density can be used to determine the number of strands that comprise a polymer. Meanwhile, apparent motion of the speckles along the polymer indicates treadmilling, in which proteins are added to one end of the polymer and simultaneously removed from the other. By patterning the supported bilayer into a checkerboard pattern of separate bilayer squares⁷⁸, the surface diffusion of MinD will be reduced; changes in the distribution of polymer lengths can be used to show whether MinD monomers are added directly from solution or after initially binding to the membrane.

Addition of purified MinE to the *in vitro* system will allow us to explore even more. First of all, the oscillatory dynamics of the *E. coli* Min system arise solely from MinD and MinE, so it is likely that we will observe periodic dynamics on the supported bilayer. The model of Huang, Meir, and Wingreen appears to be moderately accurate for the overall Min dynamics, despite its lack of a precise physical basis, so I used it to predict the dynamics of MinD and MinE on a supported bilayer (figure 6). The prediction shows rapid symmetry-breaking of the initial uniform protein coverage into small domains with and without MinD; this is followed by oscillations and gradual expansions of the domains. The experiment will show if this prediction is accurate and thus test the proposed model. Even without oscillatory dynamics, the combination of labeled MinD and MinE will show if MinE is a capping protein⁶⁸ and the extent to which MinE affects the depolymerization rate.

Another extension of essentially the same system is to replace the flat supported bilayer with a ruffled one that was recently engineered⁸². The theory that I developed on the conformations of membrane-bound polymers predicts that MinD, and several other membrane-bound polymers, will preferentially locate to regions with concave curvature. It also predicts that

polymer growth and disassembly rates will depend on the local membrane curvature. It will be exciting to see if these predictions are accurate.

Other techniques will be carried out as well. Measurements of MinD ATPase activity^{31,33,34,83} will yield several parameters that are required for modeling but are not currently known. These include the MinD nucleotide transfer rate, the dimerization constant for MinD, and the ratio of ATP hydrolysis to the number of MinD proteins released from a membrane. Also, dynamic light scattering has proven useful for rapidly assessing the binding of MinD to lipid vesicles and so may be a good way to measure binding affinities and rates. Finally, atomic force microscopy (AFM) can yield much higher resolution than light microscopy and has been useful for visualizing filaments of FtsZ⁸⁴. I plan to use AFM to investigate MinD polymers as well, hopefully while they are on a supported lipid bilayer to yield biologically meaningful results.

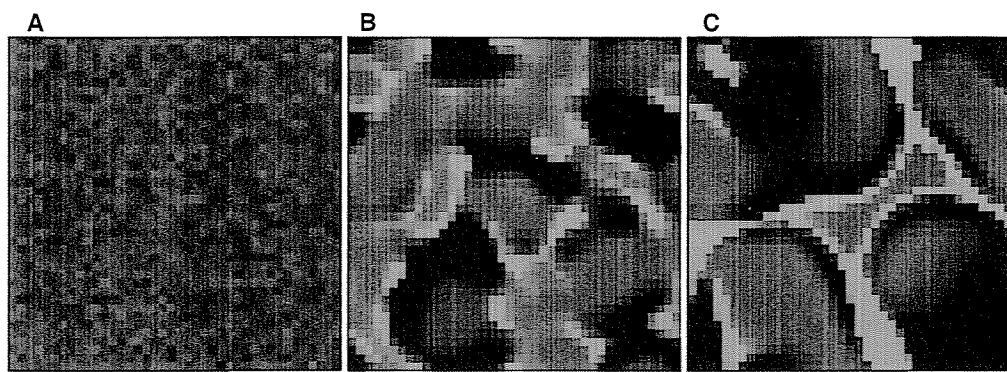


Figure 6. Dynamics of MinD and MinE on a planar supported lipid bilayer as predicted by the Huang-Meir-Wingreen model⁶⁵. Panels are 2 microns deep and 20 microns square with periodic boundary conditions. Only MinD and MinD-MinE that are bound to the membrane surface are shown: blue is MinD, red is MinD-MinE, black is neither, and pink is a mixture. The system is started (panel A) with a mixture of MinD and MinD-MinE that is uniform except for the variation that arises from the discreteness of the proteins. The system oscillates and develops structure: Panel B shows the system at 3 minutes and panel C shows the system at 7.7 minutes. *In vitro* microscopy experiments will be used to investigate this prediction.

Experimental research – *in vivo* experiments

The theoretical research and the *in vitro* experiments that I described have one primary purpose: to develop a better understanding of how the bacterial cell-division cycle works. The ultimate test for their predictions is, of course, in living cells. I plan to carry out *in vivo* experiments to firmly anchor my research program in real biology. Also, biology appears to have an endless supply of surprises which are only revealed with research on complete living systems. As with the *in vitro* work, I plan to use fluorescence microscopy as a primary research tool for studying living cells. Extensive work has been done on imaging the individual components of the Min system as well as other components of the cell-division cycle. However, much more remains to be done.

Using FRAP techniques and GFP-labeled FtsZ, it was shown that there is a high turnover of proteins in the polymer⁸⁵. I plan to carry out essentially the same experiment with GFP-labeled

MinD, which would address questions about monomer-monomer and monomer-membrane binding energies.

FRET techniques have proven to be quite useful for investigating co-localization of proteins in chemotaxis⁸⁶. I plan to apply them to several cell-division proteins. FRET between MinD and MinE will show if MinE is a capping protein, and if it binds to MinD for a prolonged period of time. FRET between MinD and MreB will show if these polymers are completely independent, which will address an on-going debate about whether the MreB coils are partially responsible for positioning the MinD coils. FRET between MinD and FtsZ will address what appears to be a paradox currently: low-resolution images show that MinD occupies the cell ends but never the middle, whereas high resolution images show that MinD is a polymer that extends from one pole to the other. Furthermore, it is not clear how the helical MinD polymer (with MinC bound to it), inhibits formation of the Z-ring.

Because of my minimal experience with imaging live cells, I will seek help from current and new collaborators. I plan to maintain my connections with the Groves lab. The Rothfield and King labs (both at the University of Connecticut Health Center) have offered *E. coli* strains with GFP-labeled Min proteins and microscopy assistance. Also, Howard Berg (Harvard) and Dyche Mullins (UCSF) have offered assistance.

Summary

I plan to study prokaryotic cell division by initially focusing on the *E. coli* Min system and gradually broadening my research scope to other *E. coli* processes and to cell division in other organisms. This system is at the heart of fundamental physical biology because it connects the physical worlds of chemistry and physics with the biological process of reproduction. Along with using cutting-edge computational and experimental methods, we will develop new ones that will help propel systems biology towards new levels of precision and rigor. The focus is not on applications but they are not far away: bacterial cell division is an obvious target for antibiotics and for bioengineering. This research program is an excellent topic for an academic laboratory because it is sufficiently focused to lend cohesion to a research group while also being rich enough to allow a variety of interesting research projects. I believe that my physical chemistry approach is ideally suited for researching these questions about organization and dynamics in bacteria.

Literature Cited

1. Gould, S.J., "Planet of the Bacteria" *Washington Post Horizon*, 119: H1, 1996.
2. Lipson, J.E.G. and S.S. Andrews, "A Born-Green-Yvon integral equation treatment of a compressible fluid" *J. Chem. Phys.*, 96: 1426-1434, 1992.
3. Kratky, O. and G. Porod, *Rec. Trav. Chim.*, 68: 1106, 1949.
4. Andrews, S.S. and A.P. Arkin, "A physical explanation for the shape of the bacterial cytoskeleton and other membrane-bound protein polymers" in preparation, 2005.
5. Andrews, S.S., S. Caron, and O.C. Zafiriou, "Photochemical oxygen consumption in marine waters: A major sink for colored dissolved organic matter?" *Limnol. Oceanogr.*, 45: 267-277, 2000.
6. Zafiriou, O.C., S.S. Andrews, and W. Wang, "Concordant estimates of oceanic carbon monoxide source and sink processes in the Pacific yield a balanced global "blue-water" CO budget" *Global. Biogeochem. Cycles*, 17: 1015, 2003.
7. Andrews, S.S., *The Measurement and Physics of Vibrational Stark Effects*, in *Chemistry*. 2001, Stanford University: Stanford, CA.
8. Andrews, S.S. and S.G. Boxer, "Vibrational Stark effects of nitriles. I. Methods and experimental results" *J. Phys. Chem. A*, 104: 11853-11863, 2000.
9. Park, E.S., et al., "Vibrational Stark spectroscopy in proteins: A probe and calibration for electrostatic fields" *J. phys. Chem. B*, 103: 9813-9817, 1999.
10. Andrews, S.S. and S.G. Boxer, "A liquid nitrogen immersion cryostat for optical measurements" *Rev. Sci. Instrum.*, 71: 3567-3569, 2000.
11. Andrews, S.S. and S.G. Boxer, "Analysis of noise for rapid-scan and step-scan FTIR difference spectroscopy" *Appl. Spectrosc.*, 55: 1161-1165, 2001.
12. *SpectFit* is an open source C language program that can be downloaded from the website <http://sahara.lbl.gov/~sandrews/software.html>. It is a general purpose curve-fitting program with many features that are unavailable in commercial applications.
13. Park, E.S. and S.G. Boxer, "Origins of the sensitivity of molecular vibrations to electric fields: Carbonyl and nitrosyl stretches in model compounds and proteins" *J. Phys. Chem. B*, 106: 5800-5806, 2002.
14. Suydam, I.T. and S.G. Boxer, "Vibrational Stark effects calibrate the sensitivity of vibrational probes for electric fields in proteins" *Biochem.*, 42: 12050-12055, 2003.
15. Park, E.S., M.R. Thomas, and S.G. Boxer, "Vibrational Stark spectroscopy of NO bound to heme: Effects of protein electrostatic fields on the NO stretch frequency" *J. Am. Chem. Soc.*, 122: 12297-12303, 2000.
16. Andrews, S.S. and S.G. Boxer, "Vibrational Stark effects of nitriles. II. Physical origins of Stark effects from experiment and perturbation models" *J. Phys. Chem. A*, 106: 469-477, 2002.
17. Treynor, T.P., S.S. Andrews, and S.G. Boxer, "Intervalence band Stark effect of the special pair radical cation in bacterial photosynthetic reaction centers" *J. Phys. Chem. B*, 107: 11230-11239, 2003.
18. Shimizu, T.S., S.V. Aksenov, and D. Bray, "A spatially extended stochastic model of the bacterial chemotaxis signalling pathway" *J. Mol. Biol.*, 329: 291-309, 2003.
19. *Smoldyn* is an open source C language program that can be downloaded from the website <http://sahara.lbl.gov/~sandrews/software.html>. It is a general purpose program for simulating chemical reaction networks with continuous spatial resolution and single molecule detail.
20. Andrews, S.S. and D. Bray, "Stochastic simulation of chemical reactions with spatial resolution and single molecule detail" *Phys. Biol.*, 1: 137-151, 2004.

21. DePristo, M.A., et al., "FRAP kinetics of the *Escherichia coli* chemoreceptor cluster analyzed by simulated diffusion" submitted, 2005.
22. Plimpton, S.J. and A. Slepoy, "Microbial cell modeling via reacting diffusive particles" *J. Phys.: Conf. Ser.*, 16: 305-309, 2005.
23. Lipkow, K., S.S. Andrews, and D. Bray, "Simulated diffusion of CheYp through the cytoplasm of *E. coli*" *J. Bact.*, 187: 45-53, 2004.
24. Hazelbauer, G.L., "Myriad molecules in motion: simulated diffusion as a new tool to study molecular movement and interaction in a living cell" *J. Bact.*, 187: 23-25, 2005.
25. Andrews, S.S., "Serial rebinding of ligands to clustered receptors as exemplified by bacterial chemotaxis" *Phys. Biol.*, 2: 111-122, 2005.
26. Andrews, S.S. and A.P. Arkin, "Simulated niche partitioning by bacteria" *Proc. Intl. Conf. on Complex Systems*, 2005.
27. Andrews, S.S. and A.P. Arkin, "Investigations of evolution and niche partitioning as optimization processes using simulated chemostat models" *In preparation*, 2005.
28. Adelman, J.L. and S.S. Andrews, "Intracellular pattern formation: A spatial stochastic model of bacterial division site selection proteins MinCDE" *Proc. Santa Fe Inst. Summer School*, 2004.
29. Margolin, W., "Bacterial sporulation: FtsZ rings do the twist" *Curr. Biol.*, 12: R391-R392, 2002.
30. Gitai, Z. and L. Shapiro, "Bacterial cell division spirals into control" *Proc. Natl. Acad. Sci. USA*, 100: 7423-7424, 2003.
31. de Boer, P.A.J., et al., "The MinD protein is a membrane ATPase required for the correct placement of the *Escherichia coli* division site" *EMBO J.*, 10: 4371-4380, 1991.
32. Hayashi, I., T. Oyama, and K. Morikawa, "Structural and functional studies of MinD ATPase: implications for the molecular recognition of the bacterial cell division apparatus" *EMBO J.*, 20: 1819-1828, 2001.
33. Hu, Z. and J. Lutkenhaus, "Topological regulation of cell division in *E. coli*. Spatiotemporal oscillation of MinD requires stimulation of its ATPase by MinE and phospholipid" *Mol. Cell*, 7: 1337-1343, 2001.
34. Lackner, L.L., D.M. Raskin, and P.A.J. de Boer, "ATP-dependent interactions between *Escherichia coli* Min proteins and the phospholipid membrane in vitro" *J. Bact.*, 185: 735-749, 2003.
35. Hu, Z., E.P. Gogol, and J. Lutkenhaus, "Dynamic assembly of MinD on phospholipid vesicles regulated by ATP and MinE" *Proc. Natl. Acad. Sci. USA*, 99: 6761-6766, 2002.
36. Hu, Z., C. Saez, and J. Lutkenhaus, "Recruitment of MinC, an inhibitor of Z-ring formation, to the membrane in *Escherichia coli*: role of MinD and MinE" *J. Bact.*, 185: 196-203, 2003.
37. Hu, Z. and J. Lutkenhaus, "A conserved sequence at the C-terminus of MinD is required for binding to the membrane and targeting MinC to the septum" *Mol. Microbiol.*, 47: 345-355, 2003.
38. Szeto, T.H., et al., "The MinD membrane targeting sequence is a transplantable lipid-binding helix" *J. Biol. Chem.*, 278: 40050-40056, 2003.
39. Zhou, H. and J. Lutkenhaus, "Membrane binding by MinD involves insertion of hydrophobic residues within the C-terminal amphipathic helix into the bilayer" *J. Bact.*, 185: 4326-4335, 2003.
40. Szeto, T.H., et al., "Membrane localization of MinD is mediated by a C-terminal motif that is conserved across eubacteria, archaea, and chloroplasts" *Proc. Natl. Acad. Sci. USA*, 99: 15693-15698, 2002.
41. Shih, Y.-L., T. Le, and L. Rothfield, "Division site selection in *Escherichia coli* involves dynamic redistribution of Min proteins within coiled structures that extend between the two cell poles" *Proc. Natl. Acad. Sci. USA*, 100: 7865-7870, 2003.

42. Suefuji, K., R. Valluzzi, and D. RayChaudhuri, "Dynamic assembly of MinD into filament bundles modulated by ATP, phospholipids, and MinE" *Proc. Natl. Acad. Sci. USA*, 99: 16776-16781, 2002.
43. Szeto, T.H., S.L. Rowland, and G.F. King, "The dimerization function of MinC resides in a structurally autonomous C-terminal domain" *J. Bact.*, 183: 6684-6687, 2001.
44. Hu, Z. and J. Lutkenhaus, "Analysis of MinC reveals two independent domains involved in interaction with MinD and FtsZ" *J. Bact.*, 182: 3965-3971, 2000.
45. Cordell, S.C., R.E. Anderson, and J. Löwe, "Crystal structure of the bacterial cell division inhibitor MinC" *EMBO J.*, 20: 2454-2461, 2001.
46. Ma, L., G.F. King, and L. Rothfield, "Positioning of the MinE binding site on the MinD surface suggests a plausible mechanism for activation of the *Escherichia coli* MinD ATPase during division site selection" *Mol. Microbiol.*, 54: 99-108, 2004.
47. King, G.F., et al., "The dimerization and topological specificity functions of MinE reside in a structurally autonomous C-terminal domain" *Mol. Microbiol.*, 31: 1161-1169, 1999.
48. Margolin, W. and R. Bernander, "How do prokaryotic cells cycle?" *Curr. Biol.*, 14: R768-R770, 2004.
49. Kruse, T. and K. Gerdes, "Bacterial DNA segregation by the actin-like MreB protein" *Trends Cell Biol.*, 15: 343-345, 2005.
50. Gerdes, K., et al., "Bacterial mitotic machineries" *Cell*, 116: 359-366, 2004.
51. Pogliano, J., "Dynamic cellular location of bacterial plasmids" *Curr. Opin. Microbiol.*, 5: 586-590, 2002.
52. Ebersbach, G. and K. Gerdes, "Bacterial mitosis: partitioning protein ParA oscillates in spiral-shaped structures and positions plasmids at mid-cell" *Mol. Microbiol.*, 52: 385-398, 2004.
53. Garner, E.C., C.S. Campbell, and R.D. Mullins, "Dynamic instability in a DNA-segregating prokaryotic actin homolog" *Science*, 306: 1021-1025, 2004.
54. Ben-Yehuda and R. Loskick, "Asymmetric cell division in *B. subtilis* involves a spiral-like intermediate of the cytokinetic protein FtsZ" *Cell*, 109: 257-266, 2002.
55. Jones, L.J.F., Carballido-López, and J. Errington, "Control of cell shape in bacteria: Helical, actin-like filaments in *Bacillus subtilis*" *Cell*, 104: 913-922, 2001.
56. Shih, Y.-L., I. Kawagishi, and L. Rothfield, "The MreB and Min cytoskeletal-like systems play independent roles in prokaryotic polar differentiation" *Mol. Microbiol.*, in press, 2005.
57. Weiss, D.S., "Bacterial cell division and the septal ring" *Mol. Microbiol.*, 54: 588-597, 2004.
58. Wu, J.L. and J. Errington, "Coordination of cell division and chromosome segregation by a nucleoid occlusion protein in *Bacillus subtilis*" *Cell*, 117: 915-925, 2004.
59. Harry, E.J., "Bacterial cell division: regulating Z-ring formation" *Mol. Microbiol.*, 40: 795-803, 2001.
60. Harry, E.J. and P.J. Lewis, "Early targeting of Min proteins to the cell poles in germinated spores of *Bacillus subtilis*: evidence for division apparatus-independent recruitment of Min proteins to the division site" *Mol. Microbiol.*, 47: 37-48, 2003.
61. Lutkenhaus, J. and S.G. Addinall, "Bacterial cell division and the Z ring" *Ann. Rev. Biochem.*, 66: 93-116, 1997.
62. Varma, A. and K.D. Young, "FtsZ collaborates with penicillin binding proteins to generate bacterial cell shape in *Escherichia coli*" *J. Bact.*, 186: 6768-6774, 2004.
63. Huang, K.C., Y. Meir, and N.S. Wingreen, "Dynamic structures in *Escherichia coli*: spontaneous formation of MinE rings and MinD polar zones" *Proc. Natl. Acad. Sci. USA*, 100: 12724-12728, 2003.
64. Howard, M. and A.D. Rutenberg, "Pattern formation inside bacteria: fluctuations due to the low copy number of proteins" *Phys. Rev. Lett.*, 90: 128102, 2003.
65. Kruse, K., "A dynamic model for determining the middle of *Escherichia coli*" *Biophys. J.*, 82: 618-627, 2002.

66. Howard, M., A.D. Rutenberg, and S. de Vet, "Dynamic compartmentalization of bacteria: accurate division in *E. coli*" *Phys. Rev. Lett.*, 87: 278102, 2001.
67. Meinhardt, H. and P.A.J. de Boer, "Pattern formation in *Escherichia coli*: A model for the pole-to-pole oscillations of Min proteins and the localization of the division site" *Proc. Natl. Acad. Sci. USA*, 98: 14202-14207, 2001.
68. Drew, D.A., M.J. Osborn, and L.I. Rothfield, "A polymerization-depolymerization model that accurately generates the self-sustained oscillatory system involved in bacterial division site placement" *Proc. Natl. Acad. Sci. USA*, 102: 6114-6118, 2005.
69. Oosawa, F. and M. Kasai, "A theory of linear and helical aggregations of macromolecules" *J. Mol. Biol.*, 4: 10-21, 1962.
70. Goldstein, R.F. and L. Stryer, "Cooperative polymerization reactions. Analytical approximations, numerical examples, and experimental strategy" *Biophys. J.*, 50: 583-599, 1986.
71. Zhao, D. and J.S. Moore, "Nucleation-elongation: a mechanism for cooperative supramolecular polymerization" *Org. Biomol. Chem.*, 1: 3471-3491, 2003.
72. Elowitz, M.B., et al., "Protein mobility in the cytoplasm of *Escherichia coli*." *J. Bacteriol.*, 181: 197-203, 1999.
73. Brass, J.M., et al., "Lateral diffusion of proteins in the periplasm of *Escherichia coli*" *J. Bacteriol.*, 165: 787-794, 1986.
74. Hall, D. and A.P. Minton, "Effects of inert volume-excluding macromolecules on protein fiber formation. I. Equilibrium models" *Biophys. Chem.*, 98: 93-104, 2003.
75. Hall, D. and A.P. Minton, "Effects of inert volume-excluding macromolecules on protein fiber formation. II. Kinetic models for nucleated fiber growth" *Biophys. Chem.*, 107: 299-316, 2004.
76. Rohwer, J.M., et al., "Implications of macromolecular crowding for signal transduction and metabolite channeling" *Proc. Natl. Acad. Sci. USA*, 95: 10547-10552, 1998.
77. Kuhn, J.R. and T.D. Pollard, "Real-time measurements of actin filament polymerization by total internal reflection fluorescence microscopy" *Biophys. J.*, 88: 1387-1402, 2005.
78. Groves, J.T. and S.G. Boxer, "Micropattern formation in supported lipid membranes" *Acc. Chem. Res.*, 35: 149-157, 2002.
79. Mileykovskaya, E., et al., "Effects of phospholipid composition on MinD-membrane interactions *in vitro* and *in vivo*" *J. Biol. Chem.*, 278: 22193-22198, 2003.
80. Sept, D., et al., "Annealing accounts for the length of actin filaments formed by spontaneous polymerization" *Biophys. J.*, 77: 2911-2919, 1999.
81. Collins, S.R., et al., "Mechanism of prion propagation: amyloid growth occurs by monomer addition" *PLOS Biology*, 2: e321, 2004.
82. Parthasarathy, R., C.-h. Yu, and J.T. Groves, "Curvature-modulated phase separation in lipid bilayer membranes" submitted, 2005.
83. Zhou, H. and J. Lutkenhaus, "The switch I and II regions of MinD are required for binding and activating MinC" *J. Bact.*, 186: 1546-1555, 2004.
84. Mingorance, J., et al., "Visualization of single *Escherichia coli* FtsZ filament dynamics with atomic force microscopy" *J. Biol. Chem.*, 280: 20909-20914, 2005.
85. Stricker, J., et al., "Rapid assembly dynamics of the *Escherichia coli* FtsZ-ring demonstrated by fluorescence recovery after photobleaching" *Proc. Natl. Acad. Sci. USA*, 99: 3171-3175, 2002.
86. Berg, H.C. and A. Vaknin, "Single-cell FRET imaging of phosphatase activity in the *Escherichia coli* chemotaxis system" *Proc. Natl. Acad. Sci. USA*, 101: 17072-17077, 2004.

Teaching Experience and Interests

Teaching is the primary reason that I am applying for a faculty position rather than for a position in industry or at a national or private laboratory. I have found teaching to be quite rewarding personally and I also believe that it is one of the greatest contributions that I can make to society.

Systems biology is a new interdisciplinary subject without a dedicated department, and very few dedicated classes. While many students have managed the transition to systems biology from either the physical or life sciences, I think that the lack of direct focus is a deficiency in modern science curricula. Meanwhile, the field is expanding rapidly. I would be excited to help fill the void by teaching undergraduate and graduate classes in systems biology, and by advising undergraduate and graduate research.

There is no shortage of topics; a few include: metabolic control analysis, allosteric interactions in multi-protein complexes, mechanics of bio-polymers and membranes, network properties of biochemical reaction networks, biological feedback control, stochastic decision-making, and systems biology software tools. I would structure an advanced course by surveying these and other topics. However, for a student to achieve a thorough introduction to systems biology, a rigorous physical and mathematical foundation is required. For this, I would suggest new courses that teach the physical concepts of thermodynamics, statistical mechanics, and mechanical engineering, all with a focus on systems biology. For example, the important topic of phase transitions could be taught with examples from lipid membranes.

Naturally, many students have other interests. I would also enjoy teaching them more traditional chemistry, physics, or biology, or other interdisciplinary topics.

Regardless of the subject, I consciously teach to several levels at once. I help students: *i.* attain course-specific knowledge for exam or real-life problems, *ii.* learn the general principles of the class material to achieve a scientific intuition, *iii.* develop scientific problem-solving skills, such as looking for characteristic time scales, and *iv.* mature as a person with hands-on laboratory work, collaborative group work, writing assignments, oral presentations, and original research. I have applied these goals to many teaching situations including ecology education for upper-elementary school children, work as a teaching assistant in university chemistry classes, mountaineering instruction for undergraduates, and the mentoring of graduate students in systems biology.

I see my role as a professor as to motivate, inspire, emphasize the important points, clarify confusing issues, and integrate the course material into the departmental program. In my experience, a good class has regular problem sets, two or three exams, and one or two major projects; these projects may include group work, laboratory work, a term paper, and/or an oral presentation. Projects are important for providing motivation and for giving students a deeper understanding of the material, as well as for teaching a heterogeneous group of students who have differing amounts of preparation. This curriculum is conventional but not complacent; the difference between a well-taught class and a poorly taught one lies in the planning of the lectures, the choice of the textbook, and the selection of problems and project topics. For evaluating the success of a class, I have found evaluation forms to be helpful for specific topics such as the choice of class material, although the observation and critiquing of my classes by fellow instructors has often been more useful. Ultimately though, there is no substitute for interacting with students on an individual basis, whether during office hours or in a laboratory.

Serial rebinding of ligands to clustered receptors as exemplified by bacterial chemotaxis

Steven S Andrews

Physical Biosciences Division, Lawrence Berkeley National Laboratory, 1 Cyclotron Road,
MS 977-152, Berkeley, CA 94720, USA

E-mail: ssandrews@lbl.gov

Received 5 May 2005

Accepted for publication 12 May 2005

Published 6 June 2005

Online at stacks.iop.org/PhysBio/2/111

Abstract

Serial ligation is the repeated reversible binding of a ligand to one receptor after another. It is a widespread phenomenon throughout biochemical systems, occurring anytime receptors are clustered together and ligand binding is reversible. Computer simulations are used in this work to investigate a representative example, which is the serial ligation of an extracellular aspartate molecule to the membrane-bound chemotaxis receptors of an *Escherichia coli* bacterium. It is found that the initial binding site of a ligand to a cluster of receptors is more likely to be near the edge of the cluster than near the middle, although there is no overall bias when all rebindings are considered. Serial ligation does not lead directly to signal amplification or attenuation but instead causes binding events to be correlated in both space and time: a ligand is likely to bind many times in rapid succession in a small region of the receptor cluster, but there can also be long intervals between bindings. This leads to an increased level of noise in the received signal but may allow a single ligand to be sensed above a uniform level of background noise. The focus of this paper is on the interpretation of simulation results so they can be generalized to a wide variety of other systems and to allow the identification of systems in which serial ligation is likely to be important. In the process, several characteristic times are identified, as are scaling laws for the spatial and temporal dynamics.

Nomenclature

Roman symbols

D	diffusion coefficient
d	average separation between receptors
k_b	binding rate constant
k_u	unbinding rate constant
N	expected number of different receptors that one ligand binds to
R	radius of receptor cluster, or of sphere for unclustered receptors
t	time
V	simulation volume

Greek symbols

ϕ	probability of geminate recombination
--------	---------------------------------------

σ_b	binding radius
σ_u	unbinding radius
$\tau_{\text{gem.}}$	characteristic time for geminate rebinding
$\tau_{\text{n.g.}}$	characteristic time for non-geminate rebinding
$\tau_{\text{ter.}}$	characteristic time for termination of rebinding
τ_{total}	typical duration of influence for one ligand
τ_u	characteristic time for unbinding

1. Introduction

Escherichia coli bacteria have a cluster of chemotaxis receptors localized to one pole of the bacterium, which are used to detect attractant and repellent molecules. There is increasing evidence that the receptors are clustered, and are coupled with several intracellular proteins, to create a highly interconnected signaling module which can respond to chemoattractants over a very wide range of concentrations

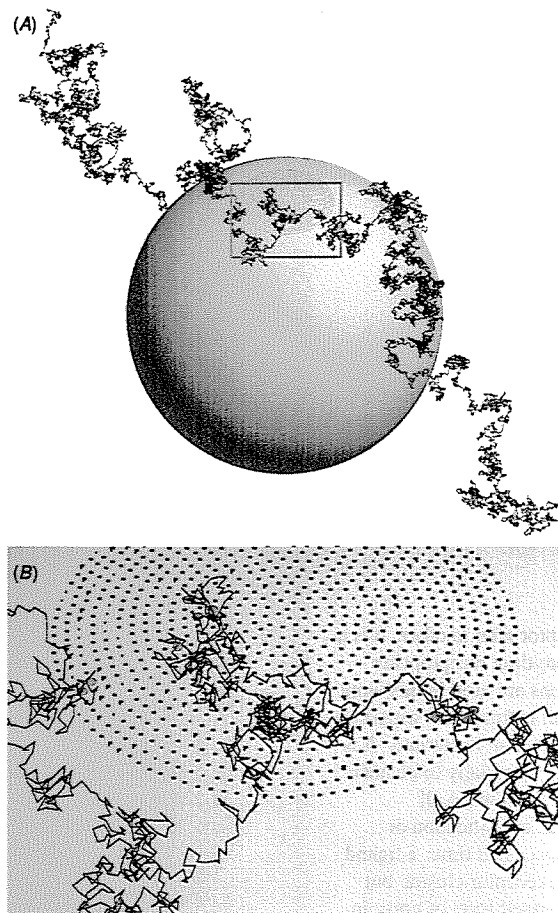


Figure 1. The model system with clustered receptors, shown as (A) the entire system and (B) a close-up view of the receptor cluster. The $1.5 \mu\text{m}$ diameter sphere represents an *E. coli* bacterium. At the top of the sphere, there are about 3000 receptors clustered together in a 450 nm diameter patch, although only 1000 receptors are shown in this figure for clarity. The Brownian motion trajectory of a single ligand is shown starting on the top left of the figure, binding to several receptors sequentially, and ending at the bottom right of the figure. Binding sites are shown in (B) with red dots.

[1]. Because ligand binding is reversible, another outcome of the receptors being clustered is that a single ligand molecule is likely to bind to several receptors sequentially (figure 1). This phenomenon, in which a molecule binds to one receptor, and then another, and another and so on, is called either *ligand rebinding* or *serial ligation*. The repeated binding of a ligand to the same receptor is called *geminate recombination* [2]. These phenomena lead to spatially and temporally correlated chemical reactions. Downstream in the signaling network, the correlated bindings may produce intermittent bursts of activity.

Correlated reactions are an important source of intracellular noise in gene expression, where the correlations arise from the sequential transcription and translation of DNA to mRNA to protein, and from sequential regulatory steps [3]. These yield short bursts of protein synthesis that

can be harmful for some cellular processes, such as circadian clocks [4], or can be beneficial for providing non-genetic individuality [5]. The ultimate origin of gene expression noise is from the discreteness of molecules, because there tend to be large relative fluctuations for molecules that are produced with low copy numbers. Serial ligation is fundamentally different: it is still the case that the noise is largest when there are few molecules and that there is stochasticity that arises from the discreteness of molecules, but now additional stochasticity arises from *Brownian motion*. Little work has been done to quantify the correlations produced by serial ligation or to determine the situations in which it is likely to be biologically important. Stochasticity and reaction correlations that arise from spatial processes are ignored by nearly all simulation algorithms, including those that are called exact [6, 7].

Most prior work on serial ligation has focused on the rebinding of ligands to an infinite planar surface that is uniformly covered with a continuous density of binding sites, leading to results that are particularly useful for surface-based experiments such as surface plasmon resonance and total internal reflection microscopy [8–12]. Other work has studied geminate recombination in detail for isolated receptor–ligand pairs [13, 14] and time-averaged binding rates for reactive patches on spheres [15–17]. The application of these studies to biological systems and to biological modeling can be unclear. More specialized studies have investigated serial ligation to T-cell receptors [18, 19] and signaling in a synaptic cleft using many ligands [20, 21].

This paper explores serial ligation for a model system that is loosely based on the *E. coli* receptor cluster, focusing on the general consequences of serial ligation and the situations in which it is likely to be biologically significant. Spatial binding patterns and temporal correlations of bindings are investigated.

2. The model system

Most of the *E. coli* chemotactic receptors are localized to a patch at a cell pole that is about 450 nm in diameter [22, 23]. The cluster contains several types of transmembrane receptors which are probably randomly mixed [24, 25] and spaced about 7.5 nm apart from each other [26, 27]. The extracellular domains of the receptors are in a densely packed 10 nm thick region between the inner and outer cell membranes called the periplasm, where they encounter attractant and repellent molecules that diffuse in from the surrounding medium. Some of these molecules, such as serine and aspartate, diffuse rapidly into the periplasm through large channels in the outer membrane while others, such as maltose and nickel ions, encounter specific binding proteins in the periplasm and then bind to receptors in this form [28].

In the model investigated here, the ordinarily rod-shaped bacterium with hemispherical ends is simplified to a $1.5 \mu\text{m}$ diameter sphere (figure 1). Receptors are arranged in either a 450 nm diameter cluster or are evenly distributed over the whole sphere to provide an unclustered reference system; the cluster radius is denoted as R . Receptors are spaced evenly along ‘latitude’ lines, where the distance between receptors on a line is equal to the distance between lines. Because

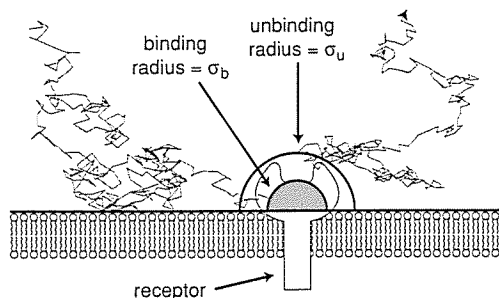


Figure 2. Details of ligand binding to a single receptor. The physical system includes the lipid bilayer and a transmembrane receptor. Heavier lines show its computational representation, comprising a smooth surface to represent the outside of the membrane and hemispheres to mark the binding and unbinding radii. A ligand binds to the receptor when it first crosses the spherical shell with radius σ_b . Subsequent unbinding is carried out by placing the ligand at distance σ_u away from the membrane surface.

of discretization effects, the receptor lattice cannot be made uniform with 3000 receptors, but instead, 3192 receptors are used for the clustered case and 3029 receptors for the unclustered case. The distance between nearest neighboring receptors (d) is about 7.2 nm and 48.1 nm, for the respective systems. Away from receptors, the surface of the sphere is a simple impermeable surface. The cell periplasm is not included in the model because preliminary results showed that it has a minimal effect on rebinding phenomena, while simultaneously complicating the discussion and reducing the generality of results.

Only a single ligand is considered at a time, both to simplify the analysis and because rebinding is likely to be most biologically significant with low ligand concentrations. Clearly, if some receptors are already occupied, then the possible consequences of the rebinding of any individual ligand will be decreased and the number of rebindings is likely to be reduced due to competition from other ligand molecules. This ligand is treated as a point-like particle with continuously variable x , y and z coordinates, which diffuses throughout the extracellular environment by simple Brownian motion. The ligand binds to a receptor at the first moment that it diffuses to within the *binding radius* (σ_b) of the receptor's center [29, 30] (figure 2). When it is subsequently released from the receptor, it is released in the direction perpendicular to the plane of the membrane, at a distance called the *unbinding radius* (σ_u), which is larger than the binding radius. These radii are derived and justified below.

All of the receptors in this model are based on the *E. coli* Tar protein and the ligand is based on aspartate, because this receptor–ligand pair has been studied thoroughly. The diffusion coefficient of aspartate (D) is about $5 \times 10^{-6} \text{ cm}^2 \text{ s}^{-1}$ [15]. Receptors are treated as though they are immobile, at least on the timescale of a simulation. The binding rate constant for aspartate to Tar (k_b) is about $10^9 \text{ M}^{-1} \text{ s}^{-1}$ [31] and the dissociation rate (k_u) is about 10^3 s^{-1} [31, 32]. These parameters are used in all simulation results presented here. The more general conclusions that are presented below were also verified using several different sets of parameters.

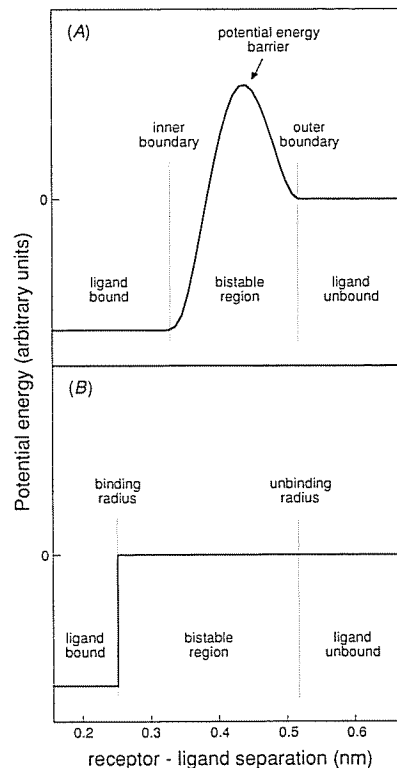


Figure 3. Interpretation of binding and unbinding radii. (A) Potential energy as a function of the distance between the receptor's active site and the center of the ligand. A ligand is considered to bind when it crosses the inner boundary and unbind when it crosses the outer boundary. (B) Simplified interaction region used in this paper. This is easy to simulate and analyze, while behaving nearly identically to the more accurate version. Binding and unbinding radii are shown with the values chosen in the main text.

3. Binding and unbinding radii, and geminate rebinding

An accurate treatment of receptor–ligand interactions would account for all the interactions that occur at short distances, such as electrostatic forces, bonding interactions and solvation effects, many of which depend on the ligand's orientation. It is conventional to simplify these to a potential energy function of a one-dimensional reaction coordinate, where this coordinate is essentially the distance between the receptor's active site and the center of the ligand (figure 3(A)) [33]. The steady-state binding reaction rate depends primarily on the height and position of the potential barrier, where the latter dependence arises from the higher probability of a ligand colliding with a large active site than with a small one. While it is tempting to use the peak of the potential energy curve to discriminate between a ligand-bound state and a ligand-unbound state, this is unsatisfactory: because the ligand moves by Brownian motion, this separation, or any other separation, is recrossed many times whenever the ligand gets close to it [34]. Instead, it is preferable to introduce bistability by not considering the

ligand to bind until it crosses a boundary on the inside of the potential barrier and then not considering it to unbind until it crosses a different boundary on the outside of the barrier. The outer boundary is the physical distance between the ligand and the active site of the receptor outside of which interactions are negligible, making it somewhat larger than a ligand radius. Once a ligand unbinds, it might rebind to the same receptor to yield a geminate recombination or it might diffuse away permanently. The probability of geminate recombination (ϕ) is clearly greater if the potential barrier is low.

The source of the reaction inhibition is simplified by eliminating the potential energy barrier and using a smaller inner boundary instead, now called the binding radius (figure 3(B)). This radius is chosen so as not to affect the steady-state binding reaction rate, which means that the probability of geminate recombination is also unchanged (both processes depend on the probability of a ligand getting from the outer boundary to the inner boundary). While the detailed dynamics on size scales smaller than the unbinding radius are affected by this substitution, it does not matter because we are only concerned with dynamics on larger distance scales, and on time scales that are longer than the time that it takes a ligand to diffuse from σ_u to σ_b (quantified below). These larger scale dynamics are essentially indistinguishable between the two models [29]. This simplification is superior to the frequently used Collins and Kimball model [13, 35, 36], in which the full potential energy barrier is replaced with an infinitesimally narrow barrier, because it is conceptually and mathematically simpler and much easier to simulate, while still yielding essentially the same results on the length and time scales that are of interest [29].

If receptor–ligand interactions occurred far from a membrane, the binding radius would be [29]

$$\sigma_b = \frac{k_b}{4\pi D}(1 - \phi). \quad (1)$$

However, receptors in the model are considered to be precisely at the surface of the membrane (figure 2), making only half of each receptor's binding surface accessible to a ligand. This leads to fewer receptor–ligand collisions by a factor of 2, leading to a corrected equation for membrane-bound receptors,

$$\sigma_b = \frac{k_b}{2\pi D}(1 - \phi). \quad (2)$$

Because of spatial symmetry, this correction does not affect the probability of geminate recombination, which is [29]

$$\phi = \frac{\sigma_b}{\sigma_u}. \quad (3)$$

As neither σ_u nor ϕ are known, they need to be estimated. Using physical arguments, it was stated that σ_u should be somewhat larger than the ligand radius (about 0.3 nm for aspartate); also, the binding of aspartate to Tar receptors has been described as nearly *diffusion limited* [31], implying that the potential energy barrier is low and thus the probability of geminate recombination is high. Consistent with this information, as well as the experimental reaction rates and diffusion coefficient listed above, the binding radius is taken to be 0.26 nm, the unbinding radius to be 0.53 nm and the probability of geminate recombination is $\phi = 0.5$.

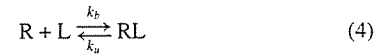
The binding radius is an artificial concept, but is still meaningful: its size is a measure of the intrinsic reactivity [37] of a receptor–ligand pair, analogous to a gas-phase collision cross-section [33]. Also, it provides a characteristic distance scale for receptor–ligand reactivity, which is not provided by the reaction rate constant, but which will prove to be an important parameter for assessing serial ligation.

4. Simulation methods

Simulations were performed with a C language computer program that uses several *Brownian dynamics* algorithms described previously [29]. Because only one ligand is considered at a time, the program could be made both fast and accurate by using adaptive time steps [38]: steps are small when a ligand is close to a receptor or the sphere surface, and large when it is far away. To yield high accuracy, the expectation displacement of the smallest diffusive steps is equal to 1% of the binding radius. Each ligand is started at a random point on a spherical shell that is just outside the surface of the sphere (plus the binding radius) because this eliminates the need to simulate the initial approach, without affecting results. A ligand escapes the system when it is 1000 sphere radii away from the sphere center, which is when its probability of ever contacting the sphere again is less than 0.1% [39] and the probability of its binding to another receptor is even lower. Collisions between the diffusing ligand and the sphere are treated with ballistic type reflections because, despite the different physical picture, this method treats Brownian motion accurately [29, 40]. Ligand unbinding is simulated using a single time step, where the length of the step is an exponentially distributed random number [41] with mean value equal to the dissociation time constant. The simulation source code can be downloaded from the World Wide Web [42].

5. Average properties and consistency checks

The chemical reaction considered here is simply



where R is a receptor and L is a ligand. As usual, the equilibrium constant is

$$K_{eq} = \frac{k_b}{k_u} = \frac{[RL]}{[R][L]}. \quad (5)$$

This can be interpreted as the equilibrium concentration ratio for many ligands, or as the time average behavior for one ligand. In either case, the system needs to be confined to a finite volume (V) so the ligands do not escape; also, it is independent of the physical locations of the receptors. Using the latter interpretation, equation (5) is rearranged to yield the ratio of time that a single ligand spends bound to a receptor, to the time that it is free,

$$\frac{\text{time bound}}{\text{time free}} = \frac{n_R k_b}{V k_u} \quad (6)$$

where n_R is the number of receptors on the cell. Using the parameters listed above, along with a volume of $9.62 \mu\text{m}^3$, the ratio is calculated to be 0.518. In a simulation that ran for 100 s of simulated time and that used the same parameters,

the ligand bound to receptors 33 837 times for a total duration of 34.1 s while it freely diffused for the other 65.9 s, which is a ratio of 0.517. In a separate simulation with unclustered receptors, the ratio was 0.512. Both ratios are within statistical error of the theoretical result.

In a separate simulation, now without a volume constraint, the probability of geminate recombination was investigated (equation (3)). Receptors were unclustered and a ligand was started at a random receptor's unbinding radius. Of 10^5 trials, 4.98×10^4 ligands underwent geminate recombination, which is a ratio of 0.498 and within statistical error of the theoretical answer of 0.5.

These results lend additional confidence in both the simulation program and in the logic used to derive equations (1)–(3).

6. Spatial dynamics

6.1. Initial and final binding locations

Suppose a ligand starts so far from a cell that it is equally likely to approach the cell from any direction. To which receptor is it most likely to bind first? In the unclustered model system where receptors are uniformly distributed over the surface of a sphere, all receptors are equivalent and the initial binding site of a diffusing ligand is as likely to be at one receptor as at another. On the other hand, there is a strong bias when the receptors are clustered (figure 4(A)). This arises from the simple fact that the middle of the receptor cluster is surrounded by the edge of the cluster, so a randomly moving ligand is likely to strike the edge before the middle.

Two analytical solutions for the initial binding site statistics are informative. If σ_b is very small relative to d , then the cluster is fairly open and the middle of the cluster is minimally 'guarded' by the edge, leading to a minimal edge effect. Alternatively, if σ_b/d is large (it can be as large as 1/2 without the binding radii overlapping), the receptors behave as a uniform disk that binds a ligand on the first contact. Solving the diffusion equation for this absorbing disk boundary condition [43, 44] leads to the result that the *probability density* (probability per area unit) for the initial binding position in the cluster is

$$p(r) = \frac{1}{2\pi R\sqrt{R^2 - r^2}} \quad (7)$$

where r is the radius of initial binding location relative to the center of the cluster. The model situation is in between these limits since σ_b/d is equal to 0.04. From simulation data, about 11% of the initial bindings were to a receptor on the edge of the cluster and about 82% of them were to a receptor in the outside half of the cluster (as a comparison, 6% of the receptors are on the edge and 75% are in the outside half).

Because a ligand's trajectory is simply a random walk, it is possible to consider it in the reverse direction as well, with the result that the final binding location follows the same probability density as the initial binding location. Thus, even if all receptors in a cluster were chemically identical, their relative locations would cause them to differ functionally: on average, the edge region is both the first and last part of the receptor cluster to bind a ligand.

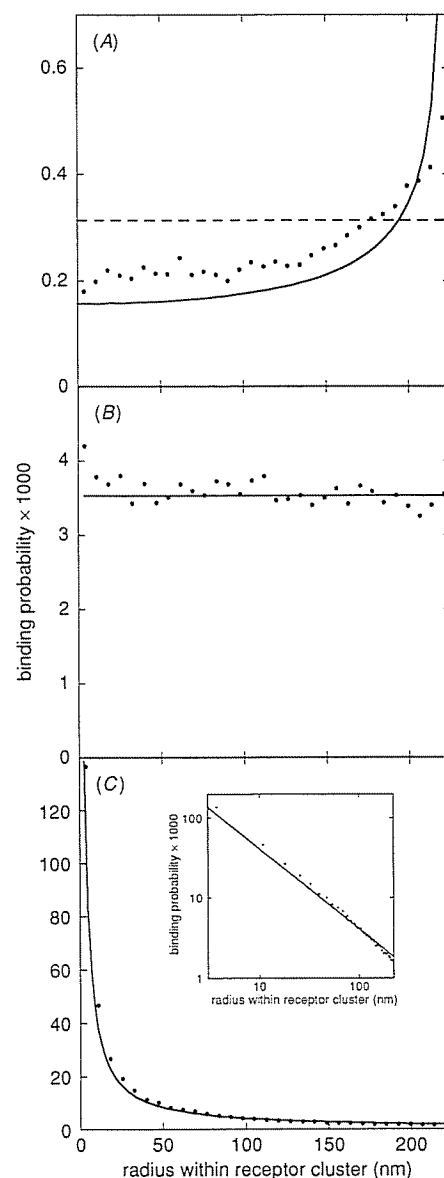


Figure 4. Spatial aspects of serial ligation with clustered receptors. In all cases, dots represent simulation data using 10^5 simulated bindings and the plots show the probability that a ligand binds to a specific receptor as a function of its distance from the center of the receptor cluster. (A) Probabilities for the initial binding site of a ligand; the solid line is the theoretical result from equation (7) for the limit of a dense receptor cluster and the dashed line is the theoretical result for a sparse receptor cluster. Integrals under all curves are 1 (including a factor of $2\pi r$ to account for the circular cluster). (B) Probabilities for every binding site of a ligand; the line is the theoretical result that there is no positional bias, scaled to have the same integrated area as the simulation result (average of 11 total bindings per ligand). (C) Spatial correlation of bindings, shown as probabilities of all binding events using a ligand started at the center of the receptor cluster; the line is proportional to r^{-1} , scaled to have the same integrated area as the simulation result. The inset is identical to panel C but shown with log-log axes.

6.2. Locations of all bindings

Is there still a statistical bias towards the edge of a cluster when every binding site is considered, rather than just the initial one? Again, there is clearly no bias for unclustered receptors because they are all equivalent. Using simulations, it is also found that there is no statistically significant bias for clustered receptors (figure 4(B)). The explanation is that binding to and unbinding from a receptor occurs in nearly the same place, so receptors have essentially no effect on the spatial trajectory of the diffusing ligand, seen qualitatively in figure 1. Binding to a receptor only delays the ligand, leaving the spatial trajectory as a simple random walk near an impermeable surface.

An implication is that a cluster of receptors (that bind reversibly) does not affect the probability of finding an unbound ligand nearby. The same result, but for many ligands, is that receptors do not affect the local concentration of unbound ligands. Statistical mechanics provides an alternate explanation for this result: the probability that a ligand is in a particular region is proportional to $\exp(-\beta E)$, where β is the Boltzmann factor and E is the potential energy [33]; outside of the receptors' binding radii, the potential energy is everywhere 0, so the unbound ligand concentration is unaffected by the presence of receptors. A second implication is that a ligand is equally likely to bind to a receptor on the edge of a cluster, in the middle of a cluster or that is relatively isolated. In this respect, all receptors in a cluster behave equivalently. Finally, on average, a ligand spends the same total amount of time bound to receptors if the receptors are clustered as if they are unclustered, a result that was already quantified in equation (6). In biology, this means that the mere clustering of receptors, without allosteric interactions, can neither amplify nor attenuate a signal that is transmitted by diffusing molecules.

6.3. Total number of bindings

Perhaps the best way to quantify the extent of serial ligation is to find the total number of receptors to which a ligand binds, on average. This is found with the integral of the simulation data in figure 4(B), including a factor of $2\pi r$ to account for the circular receptor cluster, which yields the result that ligands that bind at least once end up binding an average of about 11 total times before diffusing away permanently. Half of these are geminate rebindings because of our choice of ϕ . Removing this contribution, each ligand that binds once, binds to an average of about six different receptors over the course of its time spent in the vicinity of the cell. In contrast, it was found that ligands that bound to unclustered receptors only bound an average of three times, of which 1.5 were to different receptors. Thus, when receptors are clustered, there is an increased probability that ligands will bind multiple times; in this case, the expected number of bindings is about four times larger. Reconciling this with the prior result that receptor clustering does not affect the total number of bindings, on average, implies that four times more ligands are detected with unclustered receptors. In other words, clustered receptors lead to fewer ligands being detected and proportionately more bindings for those that are detected.

A quick calculation yields an estimate for the average total number of receptors to which a ligand binds. Starting at the center receptor and not counting geminate rebindings, the probability that a ligand ever binds to a specific nearest neighbor receptor is about σ_b/d . Considering receptors arrayed around the center one in rings that are spaced d units apart, the probability of binding to a receptor on the j th ring is about $\sigma_b/(jd)$, and this ring has about $2\pi j$ receptors. For a radius R cluster, there are about R/d rings of receptors. The expectation number of different receptors that a ligand binds to (N) is 1 for the first binding, plus the sum of the probabilities of binding to other receptors:

$$N \approx 1 + \sum_{j=1}^{j_{\max}} 2\pi j \frac{\sigma_b}{jd} \approx 1 + \frac{2\pi R\sigma_b}{d^2}. \quad (8)$$

If a ligand binds to receptor 'A', then receptor 'B' and then 'A' again, the bindings are treated here as three separate receptors, rather than as a geminate recombination. Because the initial binding is unlikely to be at the center of the cluster, this calculation overestimates the extent of serial ligation but still provides a useful estimate. Inserting the parameters used in the simulation yields about 8 and 1.5 different receptors for the clustered and unclustered cases, respectively (for the latter, the sphere radius is used for R). These are close to the simulation results of 6 and 1.5; calculated values are also in reasonable agreement with simulation results that use other values of σ_b .

Thus, the extent of serial ligation can be quantified as the expectation number of different receptors to which a ligand binds, assuming it binds at all. It depends on two unitless parameters: σ_b/d , which is the probability that a ligand hops from a receptor to its neighbor, and R/d , which is a measure of the size of the receptor cluster.

6.4. Spatial correlation

Given that a ligand binds to a specific receptor, where is it likely to bind in the future? Clearly, at each rebinding, it is more likely to bind to a receptor that is nearby than to one that is far away. The simulation result shown in figure 4(C) was created by starting many ligands, sequentially, at the center of the receptor cluster and recording the locations of subsequent bindings. These data have a profile that is slightly steeper than a curve proportional to r^{-1} , where r is the distance from the initial binding site. In a control simulation that modeled a cluster of receptors on a flat surface, the data exactly matched a slope of r^{-1} , to within statistical error, showing that the additional slope in figure 3(C) arises from the spherical surface of the modeled cell.

The r^{-1} power law can be understood by contrasting the scaling properties of ballistic motion and Brownian motion. In unrestricted three-dimensional space, consider a set of objects that start at the origin, and that move away with a constant velocity. If they produce a fixed 'mass' of trajectory behind them during each time unit, the total mass in each spherical shell about the origin is equal and, because the volume of a spherical shell is proportional to r^2 , the mass density falls off as r^{-2} . In contrast, if they move by Brownian motion, like the ligands considered here, the objects move away from

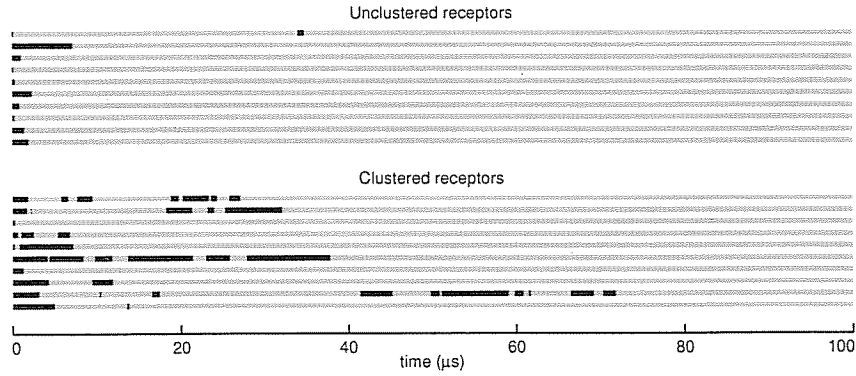


Figure 5. Ligand binding as a function of time for unclustered and clustered receptors to represent the signal that is detected by the cell. Each horizontal line represents a separate trial with time 0 defined as the moment that the ligand first binds to a receptor. Black bars represent times when the ligand is bound and gray gaps represent times when it is freely diffusing. To allow both the bound and unbound times to be seen on the same figure, the dissociation time constant was reduced from 1000 μs to 1 μs ; despite this, most geminate rebindings occurred too quickly to be resolved here.

the origin at a rate proportional to $t^{1/2}$ rather than t [45] so the mass density falls off as the square root of the previous value—now, it falls off as r^{-1} . This is unaffected by the presence of an impermeable planar membrane that includes the origin, due to symmetry. Thus, a receptor at distance r from the origin (whether it is on the membrane or not) has a probability proportional to r^{-1} of having some of the Brownian motion trajectory within its binding radius.

Restating this result for the biochemical situation, the average density of ligand bindings with receptors on a planar membrane will decrease away from the initial binding site as r^{-1} .

6.5. Domain of influence

Is there a characteristic length scale such that one can say with reasonable confidence that most bindings are within that distance of the initial binding site? For a ligand that starts at the center of the receptor cluster, the mean distance between the initial binding site and subsequent binding sites is

$$\langle r \rangle = \int_0^R 2\pi r \rho(r) dr. \quad (9)$$

The factor of $2\pi r$ accounts for the increasing circumference at larger radii and $\rho(r)$ is the density of rebindings. It was just shown that this density is proportional to r^{-1} (the relatively small effect of the curved cell surface is ignored) so the integrand is a constant and the solution is proportional to R . Although the upper limit of the integral is more complicated for ligands that start elsewhere, the result is still proportional to R . Rebindings are not localized just to the region of the first binding but are spread over the entire receptor cluster.

Alternatively, the domain of influence of a ligand could be defined as the median radius of binding, which is the radius for which half of the bindings are inside and half are outside. Again, this is found to be proportional to R . Thus, there is no characteristic length scale for rebinding: while most rebindings occur close together, enough are far apart that the spatial domain is limited only by the size of the receptor

cluster. The domain of influence of a ligand is the entire receptor cluster.

7. Temporal dynamics

7.1. Qualitative results

In the two state model of receptor activation, a receptor is ‘on’ if a ligand is bound to it or ‘off’ when no ligand is bound [46]. Suppose the bacterial chemotaxis biochemistry depends only on the cumulative signal, which is defined as the sum of the states of all receptors. Examples of this signal are shown in figure 5 using a single ligand, where a black bar indicates that the ligand is bound and a gray interval indicates that it is freely diffusing. For presentation purposes in just figure 5, k_u was increased from 10^3 s^{-1} to 10^6 s^{-1} to make the black bars a factor of 1000 shorter than they should be. In reality, an aspartate molecule spends a relatively long time bound to several Tar receptors, separated by rapid hops from one to the next.

It is seen that receptor clustering influences the number of bindings for a ligand and their relative timings. In the unclustered case, most ligands only bind once. With clustered receptors, ligands are likely to rebind quickly after each unbinding, leading to short gaps in a series of bindings. At other times, these ligands are relatively far from all receptors, leading to long gaps.

7.2. Distributions of bound and unbound time intervals

Figure 5 is interpreted by investigating the distributions of the lengths of the black bars and gray intervals. For the former distribution, unbinding follows first-order kinetics so the probability that the ligand unbinds during a short time interval is high initially and decreases exponentially. The time constant of unbinding is the inverse of the dissociation rate constant:

$$\tau_u = k_u^{-1}. \quad (10)$$

From the properties of an exponential, the average amount of time that a ligand spends bound to one receptor is τ_u and it is

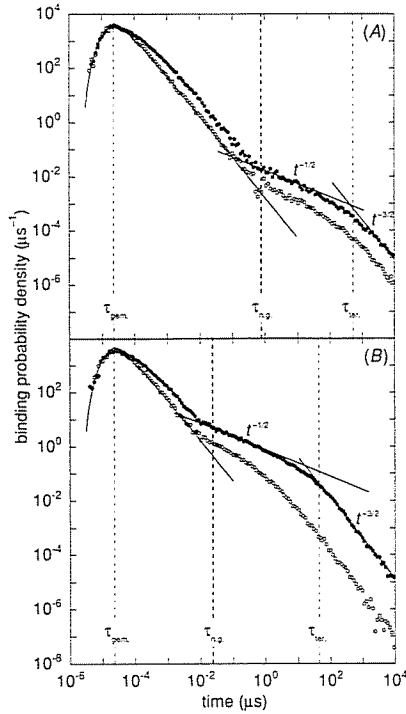


Figure 6. Temporal correlations arising from serial ligation. A ligand is released from the first receptor to which it bound at time 0 and then may rebind to the same or a different receptor at a later time. Shown is the probability density for this rebinding as a function of time for (A) unclustered and (B) clustered receptors, along with the relevant characteristic times that are discussed in the text. Open circles represent simulation data for the first rebinding and filled circles are simulation data for all rebindings. The solid lines shown in the early, intermediate and late portions of each panel are the theoretical probability density for geminate rebinding, a line with a time dependence of $t^{-1/2}$ and a line with time dependence proportional to $t^{-3/2}$, respectively. As the solid circles show the probability density of a rebinding occurring as a function of time, the integral under them is the expectation number of rebindings, which are about 2 and 10 for the unclustered and clustered cases, respectively.

rare for a single binding event to last more than several times τ_{ii} . A disproportionate number of black bars in figure 5 appear to be much longer than the $1 \mu\text{s}$ value of τ_{ii} that was used to generate the figure simply because most geminate rebinding intervals are too brief to be resolved by the printer.

The intervals between bindings are more complicated because of the fractal nature of the ligand's trajectory and because there are several possible outcomes: a geminate rebinding, a non-geminate rebinding or the ligand permanently diffusing away. Also, the statistics of the intervals are slightly different for ligands that start at the edge of the receptor cluster from those that start in the middle. The distribution of intervals between bindings is shown in figure 6.

Upon release from a receptor at time 0, a ligand is distance σ_{ii} from the geminate receptor. It cannot rebind at this moment, although it is likely to rebind soon afterwards

because the geminate receptor is only $\sigma_{ii} - \sigma_b$ distance away, which explains the initial peaks in both panels of figure 6. This portion of the data agrees with analytical results derived in the appendix (and provides an additional consistency check between simulation and theory), where it is shown that geminate rebinding is most probable at the characteristic time

$$\tau_{\text{gem.}} = \frac{(\sigma_{ii} - \sigma_b)^2}{6D}. \quad (11)$$

With the usual parameters, $\tau_{\text{gem.}} = 0.02 \text{ ns}$ for both the clustered and unclustered models. This is meaningful for the idealized system but not physically because the model is highly simplified at these small size scales. Nevertheless, the qualitative behavior is correct: the rebinding probability is very high just after unbinding and decreases for long times with a time dependence proportional to $t^{-3/2}$.

After the initial peak, the rebinding probability decreases rapidly until the ligand has had a chance to diffuse to the nearest neighboring receptors. Using the same analytical result from the appendix, non-geminate rebinding is most probable at the characteristic time

$$\tau_{\text{n.g.}} = \frac{d^2}{6D}. \quad (12)$$

These times are $\tau_{\text{n.g.}} = 0.02 \mu\text{s}$ and $0.8 \mu\text{s}$, for the clustered and unclustered models, respectively. They describe how long it takes a ligand to hop from receptor to receptor for a typical rebinding. After $\tau_{\text{n.g.}}$, a ligand is typically far enough from the geminate receptor that there is no longer a heightened probability of binding there, but it also has not diffused far enough for the edge of the receptor cluster or the sphere curvature to be dominant influences. During this period, the ligand's 'view' is of a very large array of receptors spread over a nearly planar surface, a situation that has been investigated previously [9–11, 47]. Here, the probability density of binding decreases proportionally to $t^{-1/2}$ because it is the product of: the probability that the ligand strikes the cell surface, called a *zero-crossing*, and the probability that there is a receptor at that site. The latter factor is a simple constant and the former is proportional to $t^{-1/2}$ using the theory of Brownian motion [45].

At even longer times, rebinding is terminated by the diffusion of the ligand away from the receptor cluster, or from the cell. The characteristic termination time is the average time a ligand takes to diffuse a distance equal to the radius of the receptor region,

$$\tau_{\text{ter.}} = \frac{R^2}{2D}. \quad (13)$$

For the clustered and unclustered models, $\tau_{\text{ter.}}$ is about $51 \mu\text{s}$ and $560 \mu\text{s}$, respectively; in the latter case, R is the sphere radius, as usual. Finally, the slope of the binding probability returns to $t^{-3/2}$, which can again be understood by considering the ligand's 'view'. After $\tau_{\text{ter.}}$, the ligand is typically far from the cell, so all the receptors together can be approximated as a small absorbing patch that is far away, in a situation that is analogous to the relationship between the ligand and the geminate receptor during the interval between $\tau_{\text{gem.}}$ and $\tau_{\text{n.g.}}$. This $t^{-3/2}$ dependence continues indefinitely after $\tau_{\text{ter.}}$

The characteristic times are plainly evident in figure 6 and separate several temporal regions: before any rebinding, primarily geminate rebinding, serial ligation on the whole receptor cluster and rebinding is mostly complete. Because the filled circles represent the probability density of a ligand rebinding as a function of time, the integral under the data is the expected total number of rebindings. In agreement with the values presented above, these integrals, plus 1 for the initial binding, are about 11 and 3 for the clustered and unclustered models, respectively.

7.3. Duration of influence of one ligand

From the time that a ligand first binds to a receptor, for how long does it stay around to exert an influence? This duration is simply the time that it spends bound to receptors plus the intervals between bindings, which is

$$\tau_{\text{total}} = \frac{N}{\phi} \tau_u + \tau_{\text{ter.}} \quad (14)$$

With clustered receptors, a ligand spends about 11 ms in a bound state and about 51 μs diffusing in the vicinity of the cluster, showing that the vast majority of time is spent with the ligand bound. For unclustered receptors, the results are about 3 ms with the ligand bound and 0.6 ms with it diffusing.

8. Serial ligation of intracellular proteins

On the inside of the *E. coli* plasma membrane, the array of chemotaxis receptors forms a relatively stable complex with the downstream signaling proteins CheA and CheW. There are also more transitory engagements with freely diffusing proteins, such as the methylating and demethylating enzymes CheR and CheB, which bind to individual receptors and then detach after their catalytic action is complete. Is it possible that these cytoplasmic proteins could undergo serial ligation in an analogous fashion to that just described for aspartate on the outside of the cell? This is addressed using CheR to lend a context to work on CheR binding patterns [48] and to illustrate another use of the parameters derived above.

The number of receptors and the size of the receptor cluster is the same as before, but other parameters are quite different. Rates of protein-protein association are likely to be slower than the rate constant for aspartate binding by about three orders of magnitude, with typical rates around $10^6 \text{ M}^{-1} \text{ s}^{-1}$ [49, 50]. Also, diffusion coefficients of intracellular proteins are about 200 times slower, at around $2.5 \times 10^{-8} \text{ cm}^2 \text{ s}^{-1}$ [51]. Experimental results do not help with choosing either the unbinding radius or the probability of geminate recombination, so, as a first guess, ϕ is set to 0.5, as before. This implies that σ_b is 0.027 nm and σ_u is 0.053 nm. The latter parameter is ill-defined for protein-protein interactions because of the strict orientational restrictions for binding [50], but it nevertheless would be expected to be larger than the length over which there are strong chemical interactions (figure 3). In contrast, this calculated value is less than half the length of a chemical bond, making it unlikely that ϕ is as high as 0.5. Instead, σ_u is chosen to be 0.53 nm to make it the same as it was for the previous discussion, and which is

physically reasonable, leading to values for σ_b of 0.05 nm and ϕ of 0.09. Using these parameters, the ratio σ_b/d is 0.007, which is only a one-fifth of what it was before, indicating that there will be much less serial ligation.

The enhanced likelihood of a ligand (CheR) initially binding to the edge of the cluster rather than the middle is significantly reduced here, because of this lower value of σ_b/d , and because the system geometry is now the inside of the cell membrane. Clearly, the edge only 'guards' the middle when ligands approach from oblique angles, which is made less likely due to the concave membrane curvature. As before, CheR is equally likely to bind to any receptor when all bindings are considered.

If CheR molecules were not confined to the cytoplasm, each CheR would bind to an average of about 2.3 different receptors, using equation (8), showing that the extent of serial ligation would be minimal. However, CheR proteins are indeed confined within the cell and consequently will return an essentially infinite number of times to the receptor cluster, limited only by the protein lifetime. Since a CheR is likely to diffuse a long way between binding events, the position of each binding site is largely independent of previous binding locations.

Meaningful characteristic times for CheR bindings are the unbinding time, τ_u , which is 0.1 s (based on the binding rate and the association constant of $0.09 \mu\text{M}^{-1}$ [52]), the non-geminate rebinding time, $\tau_{\text{n.g.}}$, of about 4 μs and the termination time, $\tau_{\text{ter.}}$, of about 10 ms. Comparing τ_u with $\tau_{\text{n.g.}}$ shows that, again, binding durations last very much longer than the rapid hops that a ligand makes from one receptor to another. The termination time indicates how long a CheR spends diffusing near the receptor cluster during an average encounter.

Thus, bindings of CheR to the inside of the receptor cluster are temporally and spatially correlated due to serial ligation, although not to a great extent and to a lesser degree than for extracellular bindings of aspartate. The large differences between the rates of aspartate-Tar interactions and CheR-Tar interactions imply that it is very unlikely for there to be feedback between the behaviors of specific aspartate molecules and specific CheR proteins.

9. Discussion

How does serial ligation affect a transmitted signal? From very general arguments, it was shown that receptor clustering does not lead to a higher overall level of ligand binding. Instead, some aspartate molecules are detected an average of about 11 times each, while others are completely ignored. In signal processing terms, serial ligation does not amplify a signal, but increases its contrast. This behavior makes the signal received from the receptor cluster relatively noisy, which would seem to be undesirable from an engineering standpoint, but may have a biological benefit.

It has been observed in other signaling systems that the actual duration of binding can have important effects [53]. For example, ligands with a high affinity often produce larger effects than those with low affinity even when the two are

present at the same net receptor occupancy [54]. In this case, a prolonged signal generated by the rebinding of a ligand at a cluster of receptors might generate a signal large enough to switch the state of a flagellar motor [55], allowing a single ligand to be detected over stochastic noise in the signaling system.

While serial ligation undoubtedly occurs for bacterial chemotaxis, further calculations show that it is unlikely to play a significant role. There is negligible receptor sensitivity to aspartate concentrations that are below 3×10^{-8} M [56]. This corresponds to 3% of the receptors being occupied by ligands, using the experimental dissociation constant of about 10^{-6} M [31], implying that about 90 different receptors are bound to aspartate at any time (using 3000 Tar receptors). This number is sufficiently large that correlations between binding times that arise from serial ligation will be minimal. Secondly, serial ligation effects are likely to be overwhelmed by the large allosteric effects that are enabled by receptor clustering [57, 1]. Nevertheless, in small regions of the receptor cluster, serial ligation may act in concert with allostery to yield noticeable effects; if so, this would most likely produce an evolutionary selection pressure.

Several experiments can be imagined that could investigate serial ligation for a system analogous to the one presented here. A conceptually simple one is a FRET measurement (fluorescence resonance energy transfer) with green fluorophore tagged chemotaxis receptors and red fluorophore tagged aspartate molecules. If the receptors were excited with blue light, the energy would be absorbed and then transferred to any bound ligands, which would emit in the red. As red emission would indicate a bound ligand, the time correlation function for red emission should be similar to the prediction shown in figure 6.

10. Conclusions and outlook

The dynamics of serial ligation were explored using a simple model system that is based on the binding of extracellular aspartate to the *E. coli* chemotaxis receptor cluster, which is likely to be representative of a wide variety of systems. It was found that receptor clustering, which promotes serial ligation, does not affect overall averages: a receptor is equally likely to bind a ligand if it is in a cluster or not, receptor clustering cannot lead directly to signal amplification or attenuation and clustering does not affect the concentration of free ligands in solution. Instead, serial ligation leads to binding events that are correlated in both time and space. Because of it, ligand bindings do not occur randomly, but an initial binding is likely to lead to a rapid succession of rebindings in the same region of the receptor cluster. The spatial correlation is described with a power law that is nearly proportional to r^{-1} (the minor deviation arises from the curved cell surface), which is a sufficiently broad distribution that the spatial extent of rebinding is limited only by the size of the receptor cluster. Temporal correlations are more complex, with separate characteristic times for geminate rebinding, non-geminate rebinding and the termination of rebinding. Between these characteristic times, the probability of ligand rebinding

is described well with power laws, with the probability decreasing as either $t^{-1/2}$ or $t^{-3/2}$, depending on the time period. As with the spatial correlation, the total time over which a ligand is likely to be detected is limited only by the size of the receptor cluster. Serial ligation increases in importance as the ratio of the binding radius to the separation between receptors increases, and as the size of the receptor cluster increases.

Several biological benefits have been studied for receptor clustering, such as allosteric interactions between receptors [1, 57], the enabling of molecular brachiation [48] and the reduction of cross-talk between different cell functions. All of these studies have ignored the effects of serial ligation, despite the fact that it is certain to occur in any biochemical system that includes reversible ligand binding. In many cases, including the chemotaxis example chosen, serial ligation is likely to play a minor role in the biochemical signal processing, although there are also situations where it could be important. If the noise in a signaling system is dominated by the statistics of receptor–ligand interactions, then serial ligation will lead to more noise in the system. On the other hand, if the dominant noise source is downstream of the receptor cluster, then the multiple bindings inherent to serial ligation can allow single ligands to be detected above the background level of noise.

In this work, serial ligation was simulated using a full three-dimensional model of the system which was computationally efficient because it treated only a single ligand at a time. However, this is not generally applicable so a challenge for theorists is to include the spatial and temporal correlations that arise from serial ligation in stochastic analyses of chemical networks, as well as in stochastic simulation algorithms. In their absence, even the so-called exact treatments are significantly in error.

This study on serial ligation is but one aspect of a growing awareness of stochastic effects in biochemistry. It is true that, on average, biology and chemistry behave according to analytically calculable averages, found from continuous chemical concentrations, reaction rate constants, dissociation constants and so on. However, specific systems at specific times are almost never average: a receptor is either active or inactive, a molecule is at one location and is not somewhere else and a membrane collision either did or did not happen. Biology evolves and operates in this real world of stochastic phenomena, making their understanding essential to an understanding of biology. These phenomena also introduce new challenges for scientists, requiring experimental methods that are not only more sensitive but that can also identify correlated events and computer programs that can efficiently handle the additional complexity.

Acknowledgments

This work was initiated in Dennis Bray's laboratory and completed in Adam Arkin's laboratory; both advisors provided many helpful comments. Funding was provided by NIGMS grant GM64713, the Genomes to Life project of the US Department of Energy, and by an NSF postdoctoral fellowship in biological informatics.

Appendix. Probability density for geminate rebinding

An analytic solution cannot be found for the complete temporal dynamics of serial ligation that are shown in figure 6. Instead, an exact solution for the geminate portion is calculated here, which also yields the characteristic times for geminate and non-geminate rebinding and the scaling laws for the temporal dynamics. It is found by: (i) deriving the probability density for irreversible binding to an infinite plane, and (ii) converting the result to the desired spherical system. It can also be derived from equations presented in [58].

For the planar problem, there is an infinite absorbing plane perpendicular to the x -axis at position $x = 0$. A single ligand, with diffusion coefficient D , is located on the x -axis at position $x = \sigma_u$, with the time started at $t = 0$. What is the probability density of the ligand's binding to the plane as a function of time? The result will be given as $b_{\text{pl.}}(t)$, where the subscript reflects the planar system. As there are no boundaries to the ligand's diffusion in the y or z directions, these components of the ligand's position do not influence binding to the plane and can be ignored. The spatial probability density of the ligand along the x direction is denoted by $\rho_{\text{pl.}}(x, t)$, which follows the boundary conditions and diffusion equation:

$$\rho_{\text{pl.}}(x, 0) = \delta(x - \sigma_u) \quad (\text{A1})$$

$$\rho_{\text{pl.}}(0, t) = 0 \quad (\text{A2})$$

$$\frac{\partial}{\partial t} \rho_{\text{pl.}}(x, t) = D \frac{\partial^2}{\partial x^2} \rho_{\text{pl.}}(x, t). \quad (\text{A3})$$

Equation (A1) expresses the known starting position of the ligand using a Dirac delta function ($\delta(x)$ equals infinity at $x = 0$ and 0 elsewhere, and has unit area) and equation (A2) expresses the fact that the plane absorbs any ligand that contacts it. The probability density $\rho_{\text{pl.}}(x, t)$ is undefined for negative x values because the ligand starts with a positive x value and cannot cross $x = 0$. This presents an opportunity for addressing the second boundary condition by changing the problem definition slightly to use the method of images [43, 58]: the absorbing plane is removed, $\rho_{\text{pl.}}(x, t)$ is now defined for negative x values although it is not required to be physically meaningful there and a negative delta function is added to $\rho_{\text{pl.}}(x, 0)$ at the mirror image of the positive delta function:

$$\rho_{\text{pl.}}(x, 0) = \delta(x - \sigma_u) - \delta(x + \sigma_u). \quad (\text{A4})$$

This new initial condition still satisfies the first boundary condition given above for all physically meaningful x values. The symmetry of the initial condition and the lack of directional bias during diffusion implies that $\rho_{\text{pl.}}(0, t) = 0$ at all times, meaning that the second boundary condition is satisfied as well, without requiring it as a separate constraint. The solution is now trivial: each delta function diffuses over time to become a Gaussian [39]:

$$\rho_{\text{pl.}}(x, t) = G_s(x - \sigma_u) - G_s(x + \sigma_u) \quad (\text{A5})$$

$$G_s(x) \equiv \frac{1}{s\sqrt{2\pi}} e^{-x^2/2s^2} \quad (\text{A6})$$

$$s \equiv \sqrt{2Dt}. \quad (\text{A7})$$

The probability density that a ligand binds to the absorbing plane at some time is given by the flux of $\rho_{\text{pl.}}(x, t)$ into the plane:

$$b_{\text{pl.}}(t) = D \frac{\partial}{\partial x} \rho_{\text{pl.}}(x, t) \Big|_{x=0} = \frac{\sigma_u}{t} G_s(\sigma_u). \quad (\text{A8})$$

This result is converted for the case of a spherical absorber. Now, there is an absorbing sphere centered at the origin with radius σ_b and a ligand on the x -axis at $x = \sigma_u$ at time $t = 0$. Motion tangential to the sphere surface does not affect the solution, so the problem is made rotationally symmetric by changing the initial probability density for the ligand to a uniform spherical shell, still at radius σ_u . Using r as the distance from the origin and $\rho(r, t)$ as the spatial probability density of the ligand, the boundary conditions are

$$\rho(r, 0) = \frac{1}{4\pi\sigma_u^2} \delta(r - \sigma_u) \quad (\text{A9})$$

$$\rho(\sigma_b, t) = 0. \quad (\text{A10})$$

Because the problem is rotationally symmetric, the diffusion equation is [43]

$$\frac{\partial}{\partial t} [r\rho(r, t)] = D \frac{\partial^2}{\partial r^2} [r\rho(r, t)]. \quad (\text{A11})$$

Using the substitution $\rho_{\text{pl.}}(r, t) = r\rho(r, t)$, this is identical to equation (A3), allowing us to use the solution in equation (A4), along with the new boundary conditions, to yield

$$r\rho(r, t) = \frac{1}{4\pi\sigma_u^2} [G_s(r - \sigma_u) - G_s(r - 2\sigma_b + \sigma_u)]. \quad (\text{A12})$$

The probability density flux into the sphere yields the desired result:

$$b(t) = 4\pi\sigma_b^2 D \frac{\partial \rho(r, t)}{\partial r} \Big|_{r=\sigma_b} = \frac{\sigma_b(\sigma_u - \sigma_b)}{\sigma_u t} G_s(\sigma_u - \sigma_b). \quad (\text{A13})$$

The time dependence is made clearer by expanding the Gaussian term:

$$b(t) = \frac{\sigma_b(\sigma_u - \sigma_b)}{2\sigma_u\sqrt{\pi D}} t^{-3/2} \exp\left[-\frac{(\sigma_u - \sigma_b)^2}{4Dt}\right]. \quad (\text{A14})$$

This probability density for binding is plotted in both panels of figure 5, where it is seen to be in excellent agreement with simulation data. It also yields some useful analytical results. At long times, the binding probability decreases with a dependence that is proportional to $t^{-3/2}$, which explains the scaling of the simulation data both for the time shortly before $\tau_{\text{n.g.}}$ and the time after $\tau_{\text{ter.}}$. Differentiating equation (A14) with respect to time shows that the most probable time for binding is at

$$\tau_{\text{gem.}} = \frac{(\sigma_u - \sigma_b)^2}{6D}. \quad (\text{A15})$$

This equation is used to define $\tau_{\text{gem.}}$. For the binding of a ligand to the nearest neighbor receptor, the most probable time for binding can again be found from equation (A15), but now the initial separation is the receptor spacing. This yields the $\tau_{\text{n.g.}}$ definition given in the main text. A final property of equation (A14) is that the integral of $b(t)$ over all time yields the total probability that a ligand is absorbed by the sphere rather than diffusing away permanently; the result is $\phi = \sigma_b/\sigma_u$, as stated in equation (3).

Glossary

Binding radius. The separation at which a pair of reactant molecules react with each other.

Brownian dynamics. A simulation method for molecular diffusion in which each molecule takes a step chosen from a Gaussian distribution, at each time step.

Brownian motion. Diffusive motion of a molecule that has been idealized to obey Fick's laws at all size and time scales, leading to an infinitely detailed trajectory.

Diffusion limited. Chemical reactions in which reactant diffusion is so slow that it completely determines the reaction rate.

Geminate recombination. The reaction between a pair of product molecules that arose from the same reactant molecule, back to yield a reactant. Here, it is the binding of a ligand to the same receptor from which it just dissociated.

Ligand rebinding. Synonymous with serial ligation.

Probability density. A distribution of a probability over space or time. The probability that a random variable falls within a small interval is the product of the probability density for that region and the width of the interval.

Serial ligation. A phenomenon in which a ligand sequentially binds and unbinds to many different receptors.

Unbinding radius. The initial separation between the products of a reversible reaction. It is also the physical distance between reactants outside of which interactions are negligible.

Zero-crossing. A point where a random walk crosses the plane at $z = 0$.

References

- [1] Sourjik V 2004 *Trends Microbiol.* **12** 569
- [2] Noyes R M 1955 *J. Am. Chem. Soc.* **77** 2042
- [3] McAdams H H and Arkin A 1997 *Proc. Natl Acad. Sci. USA* **94** 814
- [4] Barkai N and Leibler S 2000 *Nature* **403** 267
- [5] Arkin A, Ross J and McAdams H H 1998 *Genetics* **149** 1633
- [6] Gillespie D T 1977 *J. Phys. Chem.* **81** 2340
- [7] Meng T C, Somani S and Dhar P 2004 *In Silico Biol.* **4** 24
- [8] Agmon N and Edelman A 1995 *Biophys. J.* **68** 815
- [9] Gopalakrishnan M *et al* 2005 *Eur. Biophys. J.* at press (doi:10.1007/s00249-005-0471-2)
- [10] Lagerholm B C and Thompson N L 1998 *Biophys. J.* **74** 1215
- [11] Lieto A M, Lagerholm B C and Thompson N L 2003 *Langmuir* **19** 1782
- [12] Thompson N L, Burghardt T P and Axelrod D 1981 *Biophys. J.* **33** 435
- [13] Kim H and Shin K J 1999 *Phys. Rev. Lett.* **82** 1578
- [14] Popov A V and Agmon N 2001 *J. Chem. Phys.* **115** 8921
- [15] Berg H C and Purcell E M 1977 *Biophys. J.* **20** 193
- [16] Northrup S H 1988 *J. Phys. Chem.* **92** 5847
- [17] Shoup D and Szabo A 1982 *Biophys. J.* **40** 33
- [18] Valitutti S, Müller S, Cella M, Padovan E and Lanzavecchia A 1995 *Nature* **375** 148
- [19] Wofsy C, Coombs D and Goldstein B 2001 *Biophys. J.* **80** 606
- [20] Agmon N and Edelman A L 1997 *Biophys. J.* **72** 1582
- [21] Edelman A L and Agmon N 1997 *J. Comput. Phys.* **132** 260
- [22] Bren A and Eisenbach M 2000 *J. Bacteriol.* **182** 6865
- [23] Maddock J R and Shapiro L 1993 *Science* **259** 1717
- [24] Ames P, Studdert C A, Reiser R H and Parkinson J S 2002 *Proc. Natl Acad. Sci. USA* **99** 7060
- [25] Bourret R B and Stock A M 2002 *J. Biol. Chem.* **277** 9625
- [26] Kim S-H, Wang W and Kim K K 2002 *Proc. Natl Acad. Sci. USA* **99** 11611
- [27] Shimizu T S *et al* 2000 *Nature Cell Biol.* **2** 792
- [28] Alberts B *et al* 1994 *Molecular Biology of the Cell* 3rd edn (New York: Garland)
- [29] Andrews S S and Bray D 2004 *Phys. Biol.* **1** 137
- [30] Keizer J 1987 *Statistical Thermodynamics of Nonequilibrium Processes* (New York: Springer)
- [31] Danielson M A, Biemann H-P, Koshland D E and Falke J J 1994 *Biochemistry* **33** 6100
- [32] Dunten P and Koshland D E J 1991 *J. Biol. Chem.* **266** 1491
- [33] Atkins P W 1986 *Physical Chemistry* 3rd edn (New York: W H Freeman and Co.)
- [34] Hynes J T 1985 The theory of reactions in solution *Theory of Chemical Reaction Dynamics* ed M Baer (Boca Raton, FL: CRC Press)
- [35] Agmon N 1984 *J. Chem. Phys.* **81** 2811
- [36] Collins F C and Kimball G E 1949 *J. Colloid Sci.* **4** 425
- [37] Rice S A 1985 Diffusion limited reactions *Comprehensive Chemical Kinetics* vol 25 ed C H Bamford, C F H Tipper and R G Compton (Amsterdam: Elsevier)
- [38] Northrup S H, Allison S A and McCammon J A 1984 *J. Chem. Phys.* **80** 1517
- [39] Berg H C 1993 *Random Walks in Biology* 2nd edn (Princeton, NJ: Princeton University Press)
- [40] Edelman A L and Agmon N 1993 *J. Chem. Phys.* **99** 5396
- [41] Press W H, Flannery B P, Teukolsky S A and Vetterling W T 1988 *Numerical Recipes in C. The Art of Scientific Computing* (Cambridge: Cambridge University Press)
- [42] The source code can be downloaded from the world wide web site: sahara.lbl.gov/~sandrews/software.html.
- [43] Crank J 1975 *The Mathematics of Diffusion* 2nd edn (Oxford: Oxford University Press)
- [44] Jackson J D 1998 *Classical Electrodynamics* 3rd edn (New York: Wiley)
- [45] Mandelbrot B B 1983 *The Fractal Geometry of Nature* (New York: W H Freeman and Co.)
- [46] Bornhorst J A and Falke J J 2001 *J. Gen. Physiol.* **118** 693
- [47] Lagerholm B C and Thompson N L 2000 *J. Phys. Chem. B* **104** 863
- [48] Levin M D, Shimizu T S and Bray D 2002 *Biophys. J.* **82** 1809
- [49] Camacho C J, Kimura S R, DeLisi C and Vajda S 2000 *Biophys. J.* **78** 1094
- [50] Northrup S H and Erickson H P 1992 *Proc. Natl Acad. Sci. USA* **89** 3338
- [51] Elowitz M B, Surette M G, Wolf P-E, Stock J B and Leibler S 1999 *J. Bacteriol.* **181** 197
- [52] Yi X and Weis R M 2002 *Biochim. Biophys. Acta* **1596** 28
- [53] Shea L D, Neubig R R and Linderman J J 2000 *Life Sci.* **68** 647
- [54] Stickie D and Barber R 1991 *Mol. Pharmacol.* **40** 276
- [55] Duke T A J, LeNovère N and Bray D 2001 *J. Mol. Biol.* **308** 541
- [56] Hedblom M L and Adler J 1983 *J. Bacteriol.* **155** 1463
- [57] Bray D and Duke T 2004 *Ann. Rev. Biophys. Biomol. Struct.* **33** 53
- [58] Carslaw H S and Jaeger J C 1959 *Conduction of Heat in Solids* 2nd edn (Oxford: Clarendon)

Stochastic simulation of chemical reactions with spatial resolution and single molecule detail

Steven S Andrews¹ and Dennis Bray²

Department of Zoology, Downing Street, University of Cambridge, Cambridge CB2 3EJ, UK

E-mail: ssandrews@lbl.gov and db10009@cam.ac.uk

Received 10 March 2004

Accepted for publication 14 July 2004


Published 12 August 2004

Online at stacks.iop.org/PhysBio/1/137

doi:10.1088/1478-3967/1/3/001

Abstract

Methods are presented for simulating chemical reaction networks with a spatial resolution that is accurate to nearly the size scale of individual molecules. Using an intuitive picture of chemical reaction systems, each molecule is treated as a point-like particle that diffuses freely in three-dimensional space. When a pair of reactive molecules collide, such as an enzyme and its substrate, a reaction occurs and the simulated reactants are replaced by products. Achieving accurate bimolecular reaction kinetics is surprisingly difficult, requiring a careful consideration of reaction processes that are often overlooked. This includes whether the rate of a reaction is at steady-state and the probability that multiple reaction products collide with each other to yield a back reaction. Inputs to the simulation are experimental reaction rates, diffusion coefficients and the simulation time step. From these are calculated the simulation parameters, including the ‘binding radius’ and the ‘unbinding radius’, where the former defines the separation for a molecular collision and the latter is the initial separation between a pair of reaction products. Analytic solutions are presented for some simulation parameters while others are calculated using look-up tables. Capabilities of these methods are demonstrated with simulations of a simple bimolecular reaction and the Lotka–Volterra system.

 This article has associated online supplementary data files

(Some figures in this article are in colour only in the electronic version)

Nomenclature

Abbreviations

RDF radial distribution function (see glossary)
rms root mean square (see glossary)

Roman symbols

D mutual diffusion coefficient
 D_B diffusion coefficient for a B molecule

¹ Present address: Calvin Lab, bldg. 3-130, Physical Biosciences Division, Lawrence Berkeley National Laboratory, 1 Cyclotron Road, Berkeley, CA 94720, USA.

² Present address: Department of Anatomy, Downing Street, University of Cambridge, Cambridge CB2 3DY, UK.

$G_s(\Delta x)$ Gaussian with area of 1, mean of 0 and standard deviation of s
 $g(r)$ radial distribution function
 $\text{grn}(r, r', s)$ Green’s function for diffusion in a radially symmetric system
 $J_B(\mathbf{r}, t)$ flux of B molecules at position \mathbf{r} and time t
 k_0 rate constant for a zeroth-order reaction
 k_1 rate constant for a unimolecular reaction
 $k_{1,i}$ rate constant for the i th unimolecular reaction of a single species
 k_2 rate constant for a bimolecular reaction
 l_i initial distance of a molecule from a surface
 l_f final distance of a molecule from a surface
 $\text{Prob}(\dots)$ probability

$\text{prob}(\dots)$	probability density
$\rho_B(\mathbf{r}, t)$	spatial probability density of a single B molecule at position \mathbf{r} and time t
s	standard deviation of a Gaussian, or a mutual rms step length
s_B	rms step length of a B molecule
Δt	time step for simulation

Greek symbols

γ	boundary condition coefficient for the Collins and Kimball model
ϕ	probability of geminate recombination
$\rho_B(\mathbf{r}, t)$	number concentration of B molecules at position \mathbf{r} and time t
σ_b	binding radius
σ_u	unbinding radius

Subscripts

C	Collins and Kimball model
N	Numerical algorithm
S	Smoluchowski model, which is also the continuous time model system
a	activation limited
i	irreversible bimolecular reaction
r	reversible bimolecular reaction

1. Introduction

Computer simulations can be valuable tools for investigating chemical reaction networks, such as the complex biochemical networks that make up living systems [1–3]. They are best seen as aids to intuition, allowing one to explore the complex dynamics of reaction networks with relative ease. An aspect of this is that a simulation can rigorously determine if a proposed reaction mechanism is consistent with observed results. To mention a few examples, simulations of the *Escherichia coli* chemotaxis signaling network have yielded insights into biological robustness [4], bacterial individuality [5] and protein allostery [6].

Reaction network simulations can be classified by (i) whether they account for spatial information and (ii) whether they include the stochasticity that arises from discrete molecules rather than continuous chemical concentrations. With greater levels of detail, the results become more accurate but the simulations take longer to execute and require more experimental parameters. The algorithms presented in this work are in the most detailed category of this classification scheme, accounting for both stochastic and spatial information. This high level of accuracy is applicable to a wide range of systems but is especially useful for biology, where there can be a high degree of spatial organization [7, 8] and key molecular species often exist with low copy numbers [5, 9]. As an example, a reaction network that includes membrane ion channels is highly sensitive to the stochasticity that arises from individual molecules and spatial influences.

The drawbacks of the high level of detail were reduced as much as possible by designing the algorithms to be computationally efficient and to require few parameters.

The fundamental processes for which algorithms are presented are as follows: molecular diffusion, interactions of molecules with surfaces, zeroth-order chemical reactions (the spontaneous introduction of new molecules into the system, which is physically impossible but computationally useful), unimolecular chemical reactions and bimolecular chemical reactions. In all but the last case, the algorithms yield results that are in exact accord with those of a simplified model system. However, achieving the same accuracy for bimolecular reactions would make a simulation too slow to be useful. Instead, we present a fast alternative method and show that it yields results in good agreement with analytical models.

Our algorithms have been implemented in a C language computer program called *Smoldyn* (for *Smoluchowski dynamics*) which may be downloaded from the World Wide Web. Another publicly available computer program that works at a similar level of detail is *MCell*, which was originally developed to model signaling in neuromuscular junctions [10], although it works at a lower level of spatial resolution and it has the limitation that bimolecular reactions can only be simulated at surfaces.

2. The model system

In this section, real chemical processes are simplified to a precisely defined model system. Our model is an extension of the *Smoluchowski model* for *diffusion-influenced* systems [11], which is presented here as well.

In the model, time increases continuously, as it does in nature, but in contrast to the finite time steps that are introduced in the next section for the simulation algorithms. Each molecule is treated as a point-like particle that diffuses freely in space with continuously variable x , y and z coordinates, quantified with Fick's laws [12]:

$$\mathbf{J}_B(\mathbf{r}, t) = -D_B \nabla \rho_B(\mathbf{r}, t) \quad (1)$$

$$\dot{\rho}_B(\mathbf{r}, t) = D_B \nabla^2 \rho_B(\mathbf{r}, t). \quad (2)$$

B is some generic chemical species, $\mathbf{J}_B(\mathbf{r}, t)$ is the flux of B molecules at position \mathbf{r} and time t , $\rho_B(\mathbf{r}, t)$ is the local number concentration of B molecules, and D_B is the diffusion coefficient for B [13]. The coordinates of a molecule are its center of mass. The Smoluchowski description also accounts for external and long-range forces (such as between ionic species [14]) but we ignore them because they have minimal influence in a typical biochemical system and they are computationally expensive to simulate. To allow the use of Fick's laws on small size scales as well as large ones, the dynamics of the solvent and other unreactive species are ignored [15], leading to infinitely detailed *Brownian motion* of the reactive molecules. This approximation makes the results only accurate on size scales that are somewhat larger than those of individual molecules. Similarly, steric interactions are ignored between molecules that do not react with each other, which is valid for dilute solutions. Molecular spatial

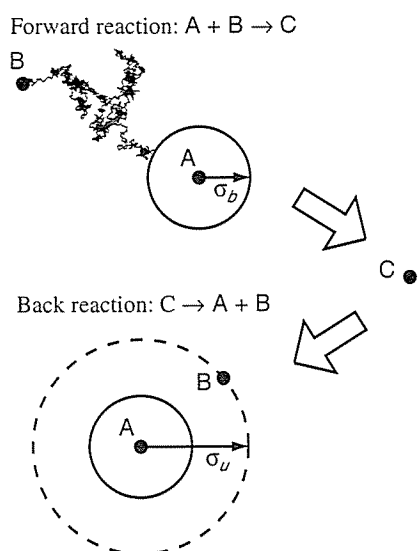


Figure 1. Forward and back reactions in the physical model for the reaction $A + B \leftrightarrow C$, shown from the standpoint of an A molecule. A forward reaction occurs when the centers of an A and a B molecule (black dots) diffuse to a separation that is equal to the binding radius, σ_b (circle with solid line), forming a C molecule. When a back reaction occurs, the A and B products are initially separated by the unbinding radius, σ_u (circle with dashed line), which is made larger than the binding radius so as to prevent the instant recombination of the products. The angular location of B is random due to rotational diffusion. The same method is used for the numerical algorithms presented in this paper although, for computational efficiency, diffusion is simulated with relatively long steps and the sizes of the binding and unbinding radii are modified so as to yield quantitatively accurate reaction rates.

orientations and internal energy levels typically fluctuate on time scales that are faster than the diffusive and reactive processes that are of interest [14, 16], allowing them to be ignored as well. Because of these approximations, the complete time-dependent state of the model is fully specified by a list of the molecular positions.

By definition, a *diffusion-limited* bimolecular reaction occurs very rapidly once two reactive molecules come into contact, which happens when the molecular centers are separated by a distance equal to the sum of the molecular radii. This description is used for the Smoluchowski model in which a bimolecular reaction occurs at the moment when two reactive molecules collide with each other. Smoluchowski derived the steady-state reaction rate for this physical description, in terms of the molecular radii and the diffusion coefficients [11]. However, most reactions occur at a slower rate because of a reaction activation energy. This is addressed in the Smoluchowski model by replacing the sum of the molecular radii with a smaller effective *binding radius* (σ_b), thus yielding the correct steady-state reaction rate for all bimolecular reactions, regardless of the reaction mechanism (see figure 1). This binding radius is derived below.

Reversible reactions, such as the generic reaction $A + B \leftrightarrow C$, pose a problem. If the A and B products of the

backward reaction are initially separated by the binding radius, which is the obvious separation, then the ensuing Brownian motion of A and B makes them almost certain to collide again. This leads to a nearly instantaneous reaction back to C, which is clearly not acceptable. (The terms ‘almost’ and ‘nearly’ are understatement since the actual probability for recollision is 1 and the expected time that elapses before reacting is 0 [17]. Qualitatively, an initial separation of σ_b implies that any net motion of the molecules towards each other yields a reaction, which is nearly certain because true Brownian motion has an infinite number of random walk steps in a finite time period; all but a vanishingly small portion of the possible random walks include at least a little net motion of the molecules towards each other.) This recollision problem is not addressed in the Smoluchowski model because it does not consider reversible reactions. The related *Collins and Kimball model* solves the problem by replacing the rule that reactions always occur upon collision with one in which there is a certain probability of a reaction at each collision [17, 18]. While useful mathematically, this confuses the physical picture because a single collision almost certainly leads to infinitely more collisions, implying that the probability of reaction at each collision must be infinitesimal. For ease of simulation, our scheme is closer to the spirit of the Smoluchowski model: the A and B dissociation products are initially separated by a fixed distance which is larger than σ_b , called the *unbinding radius* (σ_u) [19]. Using this rule, neither inter-molecular forces nor reaction probabilities need to be introduced, leaving diffusion as the sole fundamental process. After unbinding, the A and B product molecules may diffuse away from each other or they may diffuse together again and rebind, called a *geminate recombination* [14, 20].

An unbinding radius is an artificial concept but its use can be justified. Physically, a C molecule is an A–B complex, for which the interaction potential energy is a function of the A–B separation, typically with an activation barrier [21]. If diffusion influences the system even a small amount, any boundary between reactants and products may be crossed many times. To prevent this, it is helpful to introduce bistability by defining a boundary on each side of the activation barrier: a forward reaction occurs when the A–B separation is less than the inner boundary and a reverse reaction occurs when it is greater than the outer boundary [22]. The model defined here does not have an activation barrier, although we retain the two boundaries.

Most aspects of this model on size scales of individual molecules or smaller are incorrect, such as infinitely detailed Brownian motion, the assumption that molecules do not have excluded volume, and reaction dynamics with fixed binding and unbinding radii. However, all aspects of the model are qualitatively correct on larger size scales because macroscopic diffusion does follow Fick’s laws and reactions only occur between physically proximate molecules. It becomes quantitatively accurate when the model is supplemented with experimental data, including diffusion coefficients and reaction rates.

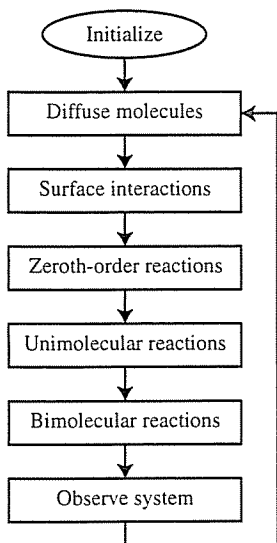


Figure 2. Flowchart for our simulation program *Smoldyn*. Alternating diffusion and bimolecular reactions are an essential aspect of the bimolecular reaction algorithm.

3. Simulation algorithms

In this section, the model is converted from a simplified description of physical processes to numerical algorithms. To do this, the continuous time of the model is replaced with steps of length Δt , which can be kept constant throughout the simulation [23] (which is done in *Smoldyn*) or made adaptive so as to focus computational effort on important time segments [24]. Either way, it is helpful to think of the end of each step as an observation of a virtual system that evolves continuously. In particular, molecules are considered to move with infinitely detailed Brownian motion, even though the detail is neither explicitly simulated nor observable. Using this interpretation, these algorithms are designed to yield observable results that are as close as possible to the analytically derived dynamics of the model system. The simulation errors can be made arbitrarily small because the simulated dynamics become identical to those of the model in the limit of small time steps. Except for the bimolecular reaction one, each algorithm can be called ‘exact’ because the simulated results are also identical to those of the model for arbitrarily long time steps in the absence of coupling with other processes.

A conventional program framework is used here, in which the program has some initialization procedures and then runs a loop over time steps (figure 2). During each iteration of the loop, several processes are simulated independently, described below in turn. See appendix A for implementation details.

3.1. Molecular diffusion

Because the model considers individual molecules rather than concentrations, Fick’s second law (equation (2)) is rewritten as a master equation by replacing the number density of B

molecules with the spatial probability density for a single molecule:

$$\dot{p}_B(\mathbf{r}, t) = D_B \nabla^2 p_B(\mathbf{r}, t) \quad (3)$$

The product $p_B(\mathbf{r}, t) d\mathbf{r}$ is the probability that a specific B molecule is within volume $d\mathbf{r}$ about position \mathbf{r} at time t . In a simulation, a molecule starts at a known position and diffuses over the course of a time step. Solving equation (3) for this initial condition shows that the probability density for the displacement of a molecule after a time step has a Gaussian profile on each Cartesian coordinate [12, 25]:

$$p_B(\mathbf{r} + \Delta\mathbf{r}, t + \Delta t) = G_{s_B}(\Delta x) G_{s_B}(\Delta y) G_{s_B}(\Delta z) \quad (4)$$

$$G_s(\Delta x) \equiv \frac{1}{s\sqrt{2\pi}} \exp\left(-\frac{\Delta x^2}{2s^2}\right) \quad (5)$$

$$s_B \equiv \sqrt{2D_B\Delta t} \quad (6)$$

where Δx , Δy and Δz are the Cartesian displacements, $G_s(\Delta x)$ is a normalized Gaussian with mean 0 and standard deviation equal to s , and s_B is the *root mean square (rms) step length* of species B. These results form the basis of a simulation method called *Brownian dynamics* [26, 27] in which diffusion is simulated by picking a normally distributed random displacement for each molecule at each time step.

3.2. Treatment of surfaces

Nearly all physical reaction systems are confined to a finite volume, making it necessary to simulate surface interactions. Surfaces are most easily treated as arrays of flat panels which might be as simple as the square walls of a cubical reaction volume or as complex as the membranes of a neuromuscular junction [10]. From a computational viewpoint, surface types include the following: inert impermeable surfaces, which prevent molecules from passing from one side to the other; periodic boundaries of the simulation volume (also called toroidal boundaries), which do not exist physically but are useful for the simulation of systems with effectively infinite extent; and absorbing surfaces, which irreversibly capture all molecules that diffuse into them. In each case, the algorithm has to determine whether each molecule interacted with each panel of the surface during the previous time step using the standard criterion that all observable dynamics should be indistinguishable from those of the model.

Impermeable surfaces are considered first. Solving equation (3) with an impermeable plane as a boundary condition shows that the spatial probability density, $p_B(\mathbf{r}, t)$, reflects off the surface like light from a mirror [25]. Thus, even though molecules are assumed to move exclusively by Brownian motion over the course of a time step and the surface may be quite rough on a microscopic scale, diffusion in the presence of inert impermeable surfaces is accurately simulated using ballistic-type reflections [26]. In the algorithm, each molecule is propagated forward over Δt according to equation (4); then, the straight line path of the molecule is reflected off any surface that it crosses.

Periodic boundaries are similar. Because equation (4) is correct in the absence of surfaces, it is also correct for

periodic boundaries, provided that any probability density that escapes the system is translated across the simulation volume. In the algorithm, any molecule that diffuses past a boundary is transferred across the system as though it had followed a straight line over the course of the time step.

An absorbing surface is treated by temporarily considering it to be permeable and asking the question: what is the probability that a specific molecule crossed the surface during the time step? If the molecule started on the inside and diffused to the outside, then it obviously crossed the surface and should be absorbed. It could also start and end on the inside but have crossed the surface during the time step, the probability of which can be found using the initial and final perpendicular distances to the surface, denoted by l_i and l_f , respectively (these are positive if the molecule is inside and negative if it is outside). The probability that the molecule crossed the surface at least once, starting from distance l_i , conditioned with the additional knowledge of l_f , is

$$\begin{aligned} \text{Prob}(\text{cross}|l_f) &= 1 - \text{Prob}(\text{no cross}|l_f) \\ &= 1 - \frac{\text{prob}(\text{no cross}, l_f)}{\text{prob}(l_f)}. \end{aligned} \quad (7)$$

$\text{Prob}()$ is a probability, $\text{prob}()$ is a probability density, a vertical line indicates a conditional probability, and a comma indicates a joint probability [28]. For example, $\text{Prob}(\text{cross}|l_f)$ is the probability that the boundary is crossed, given a knowledge of l_f , and $\text{prob}(\text{no cross}, l_f) dl$ is the probability that the boundary is not crossed and the final distance is between l_f and $l_f + dl$. The densities are found with equation (3) and the initial condition that the molecule starts at l_i away from a surface [25]. For the joint density, a boundary condition is that the probability that the molecule is at the surface is 0. Results are

$$\text{prob}(\text{no cross}, l_f) = G_{s_B}(l_f - l_i) - G_{s_B}(l_f + l_i) \quad (8)$$

$$\text{prob}(l_f) = G_{s_B}(l_f - l_i). \quad (9)$$

Substituting these into equation (7) yields the desired answer:

$$\text{Prob}(\text{cross}|l_f) = \exp\left(-\frac{2l_i l_f}{s_B^2}\right). \quad (10)$$

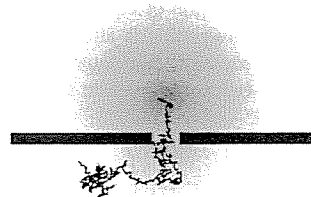
Thus, the algorithm for absorbing surfaces is that a molecule should be absorbed if it ends up on the far side of the surface at the end of a time step or if a random number with a uniform distribution between 0 and 1 is less than $\exp(-2l_i l_f / s_B^2)$.

All of these methods are exact for planar surfaces but are in error for curved surfaces or near junctions of flat surface panels. An example is a pore in a membrane (figure 3): using the continuous time model, a molecule might curve around after going through the pore, but the diffusion algorithm only allows molecules to travel in straight lines during time steps. In general, the spatial resolution is approximately the molecular rms step length.

3.3. Zeroth-order reactions

A zeroth-order reaction progresses at a rate that is independent of all chemical concentrations, implying that product molecules are formed spontaneously. While unphysical, zeroth-order reactions can be useful components

Model: detail is infinite



Simulated: detail ~ rms step length

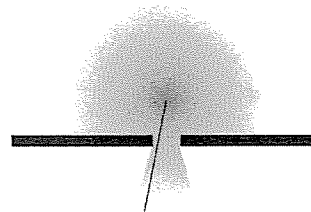


Figure 3. Example of limited spatial resolution in the simulation. The top panel shows diffusion through a pore in a membrane (gap in black bar) using the model system. The molecule starts above the pore. The thin black line shows a representative molecule trajectory and the shading represents the probability that the particle ends at each location. The lower panel presents the same information for the simulation, where it is seen that the probability density below the pore is incorrect due to the use of finite length time steps and straight line trajectories. Accurate results would require a shorter time step.

of simulations because they can provide chemical inputs to the simulated system without requiring a complete treatment of the input mechanism. For example, a chemical reactor might have an input port that continuously adds a chemical, or a biological cell may include a protein that is synthesized by biosynthetic pathways that are not of immediate interest. In both cases, these could be treated explicitly, or they could be simulated using a zeroth-order reaction to produce exactly the same result.

If the product of the reaction is A and k_0 is the rate constant, the zeroth-order mass-action rate law is

$$\dot{\rho}_A = k_0. \quad (11)$$

On average, $k_0 \Delta t$ product molecules are formed during each time step. However, this has some stochastic variation, which is given with a Poisson distribution [28].

3.4. Unimolecular reactions

Unimolecular reactions are described by the generic equation $A \rightarrow \text{products}$. This might describe a true unimolecular reaction, such as a molecular dissociation, or a bimolecular reaction between an A molecule and an abundant species that is not explicitly simulated. The kinetics are typically of first-order:

$$\dot{\rho}_A = -k_1 \rho_A \quad (12)$$

where k_1 is the first-order rate constant. Upon integration, the probability that a specific A molecule reacts during Δt is

$$\text{Prob}(\text{reaction}) = 1 - \exp(-k_1 \Delta t). \quad (13)$$

If an A molecule can react via multiple first-order pathways, a sequential application of equation (13) leads to a bias towards the first pathway that is attempted. Instead, solution of a collection of equations like equation (12), where the i th reaction has a first-order rate constant $k_{1,i}$, leads to the reaction probabilities [10]:

$$\text{Prob}(\text{reaction } i) = \frac{k_{1,i}}{\sum_j k_{1,j}} \left[1 - \exp \left(-\Delta t \sum_j k_{1,j} \right) \right]. \quad (14)$$

The efficient simulation of these equations is discussed in appendix A.

3.5. Bimolecular reactions

Bimolecular reactions, described by the generic equation $A + B \rightarrow C$, have the steady-state reaction rate:

$$\dot{\rho}_C = k_2 \rho_A \rho_B \quad (15)$$

where k_2 is the second-order rate constant, from which it is possible to find the binding radius of the model. An exact algorithm would be based on a question similar to that posed above for absorbing surfaces: given the positions of molecules A and B before and after a time step, what is the probability that the distance between them was less than the binding radius at some point during the time step? Equations analogous to equations (7) to (10) can be written and solved for this situation (they are derivable from equations presented in chapter 14 of [29]). However, the most simplified result still requires a numerical integral, making it too computationally expensive for simulations. Even a transcription of the result to a look-up table requires a very large table, four-dimensional interpolation (initial separation, final separation, interior angle and binding radius), and still requires many calculations for every potential collision at every time step. Unlike the other algorithms, an exact solution for bimolecular reactions is not practical. However, there may be reasonably efficient simulation methods if one abandons the intuitive representation presented here, along with the option of using constant size time steps [30, 31].

Because of these difficulties, we temporarily ignore the theory and choose an algorithm that is intuitive, simple and very fast: two molecules always react if they end up within $\sigma_b(\Delta t)$ at the end of a time step and never react if the final separation is greater than that. For reversible reactions, dissociation products are initially separated by $\sigma_u(\Delta t)$. These parameters are analogous to the binding and unbinding radii of the model system (figure 1) and approach them in the limit of small time steps. They are derived in the next section and the resulting dynamics are investigated in the following section.

4. Bimolecular reaction parameters

The correct binding radius for the simulation is, quite simply, that value which makes the simulated bimolecular reaction rate equal the experimental rate. The latter is presumed known, so we derive the simulated reaction rate in terms of the binding

radius, equate it to the experimental rate constant, and invert the result to yield the binding radius. Unfortunately, the derivation is complicated.

The first complication occurs in deciding which experimental reaction rate to use. As usual, the chemical equation is $A + B \rightarrow C$. Suppose we start with a *well-mixed* distribution of reactants, which is one in which the molecules have random positions but with the constraint that no A–B pairs are allowed to be closer than a binding radius of each other. As we observe the subsequent reactions, we see that the reaction rate ‘constant’ given in equation (15) is not actually constant but is extremely high initially, because of A–B pairs that happen to start close to each other, and then decreases and approaches a *steady-state* value [11, 14, 32]. This steady-state value is nearly always the one that is reported as the experimental reaction rate. Thus, our approach is to find the binding radius which makes the simulation, using a steady-state distribution of A and B molecules, reproduce the reported reaction rate. The resulting binding radius is a parameter of the model, so it is equally applicable at steady-state *and* away from steady-state.

In these derivations, separate equations are found for (i) the dynamics that arise from the analytical model that was defined in the section 2 and which is based on Smoluchowski dynamics and (ii) those that arise from the numerical algorithms. In cases where equations differ between the Smoluchowski based model and the numerical algorithm, they are labeled with subscripts ‘S’ and ‘N’, respectively. Additionally, the subscripts ‘i’ and ‘r’ are used to distinguish results for irreversible and reversible reactions. Look-up tables and source code are available as supplementary information³, as described at the end of the text.

4.1. Irreversible reactions. Smoluchowski model

The *radial distribution function* [33] (RDF, $g(r)$) between A and B molecules is the average distribution of distances between A and B molecules. More precisely, $\rho_B g(r) dr$ is the probability that there is a B molecule within a small volume element dr at distance r from any specific A molecule, where ρ_B is the overall number density of B. Because A and B molecules react when they collide, $g(r)$ equals 0 for $r < \sigma_b$. Any influence between A and B molecules diminishes for large separations, so $g(r)$ approaches 1 as r tends to infinity. While it is conceptually possible to start a chemical system with nearly any shape RDF, the Smoluchowski RDF for irreversible reactions always approaches the steady-state solution [14] (figure 4(A)):

$$g_{Si}(r) = 1 - \frac{\sigma_b}{r}, \quad r > \sigma_b. \quad (16)$$

The depletion of B molecules around A molecules arises not from any long-range interaction, but because reactive species that are close together are likely to react, which excludes them from the average [17].

The reaction rate is the net flux of B molecules towards A molecules, which is calculated using equation (3) and the

³ Supplementary data files are available from stacks.iop.org/PhysBio/1/3/001.

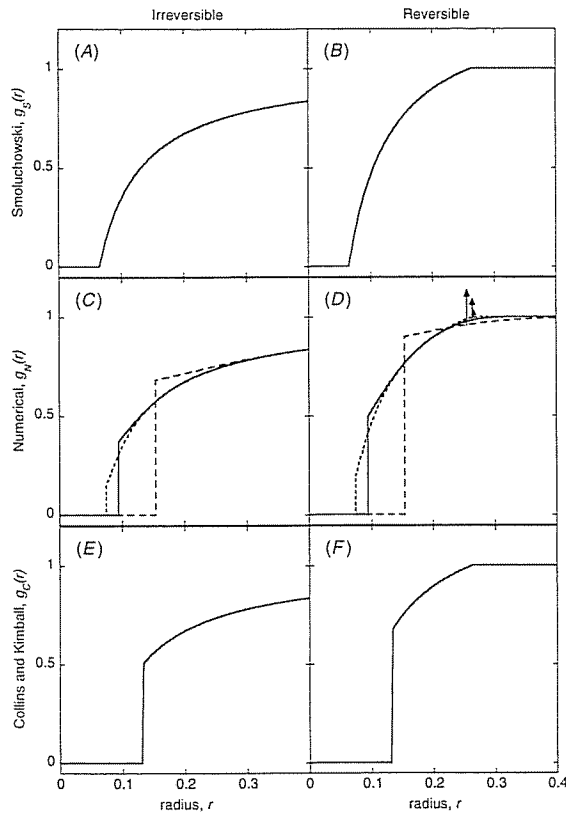


Figure 4. Radial diffusion functions (RDFs) for bimolecular reactions at steady-state with various models. Diffusion coefficients are $10^{-8} \text{ cm}^2 \text{ s}^{-1}$ for each reactant and rate constants are $10^6 \text{ M}^{-1} \text{ s}^{-1}$ for irreversible reactions. For reversible reactions, geminate recombination probabilities are 0.25 and rate constants are increased to $1.3 \times 10^6 \text{ M}^{-1} \text{ s}^{-1}$ to account for geminate reactions (equation (28)). (A) Smoluchowski model (equation (16)) with $\sigma_b = 0.066 \text{ nm}$. (B) Smoluchowski model (equation (29)) with $\sigma_b = 0.066 \text{ nm}$ and $\sigma_u = 0.264 \text{ nm}$. (C) Numerical algorithm with $\sigma_b = 0.075 \text{ nm}$, $s = 0.049 \text{ nm}$, $k_{Ni} = 2 \times 10^6 \text{ M}^{-1} \text{ s}^{-1}$, and $\Delta t = 0.61 \text{ ns}$ for the solid line; other lines use time steps that are 0.061 and 6.1 ns, shown with short and long dashes, respectively. (D) Lines are the same as those in (C) but for reversible reactions; for the solid line, $\sigma_u = 0.264 \text{ nm}$. Arrows represent Dirac delta functions at the unbinding radii. (E) Collins and Kimball model (equation (33)) with $k_{Ca} = 2 \times 10^6 \text{ M}^{-1} \text{ s}^{-1}$ and $\sigma_b = 0.132 \text{ nm}$. (F) Collins and Kimball model (equation (35)) with $k_{Ca} = 2 \times 10^6 \text{ M}^{-1} \text{ s}^{-1}$, $\sigma_b = 0.132 \text{ nm}$ and $\sigma_u = 0.264 \text{ nm}$. Note that the RDF for the numerical algorithm approaches the Smoluchowski RDF for short time steps, a well-mixed RDF (a step function) for long time steps, and is qualitatively similar to that of the Collins and Kimball model.

definition of the RDF. The general reaction rate for models in which time is treated continuously and its solution for the Smoluchowski model at steady-state are, respectively,

$$\dot{\rho}_C = 4\pi\sigma_b^2 D\rho_A\rho_B \left. \frac{\partial g(r)}{\partial r} \right|_{\sigma_b} \quad (17)$$

$$\dot{\rho}_C = 4\pi D\sigma_b\rho_A\rho_B \quad (18)$$

Here D is the *mutual diffusion coefficient* [34], defined as $D_A + D_B$. The proportionality of the reaction rates to ρ_A and ρ_B is the same as in the second-order rate equation, leading to the well-known solution of the rate constant for irreversible reactions according to the Smoluchowski model [11]:

$$k_{Si} = 4\pi D\sigma_b. \quad (19)$$

This rate is limited only by diffusion, so k_{Si} is the diffusion-limited rate constant.

4.2. Irreversible reactions, numerical algorithm

In the limit of short simulation time steps, the diffusion simulated by Brownian dynamics approaches the infinitely detailed Brownian motion that the model assumes. Thus, in this limit, the numerical reaction rate constant, k_{Ni} , is equal to the Smoluchowski result in equation (19). Solving the equation for σ_b , which is the only necessary simulation parameter (the notation $\sigma_b(\Delta t)$ was simplified to just σ_b), yields a solution that is valid whenever the *mutual rms step length* is much smaller than the binding radius; the mutual rms step length is defined as $s = (2D\Delta t)^{1/2} = (s_A^2 + s_B^2)^{1/2}$. It is instructive to see when this solution can be used. A typical reaction rate for proteins is $10^6 \text{ M}^{-1} \text{ s}^{-1}$ and protein diffusion constants are typically at least $10^{-8} \text{ cm}^2 \text{ s}^{-1}$. These are substituted into equation (19), and then equation (6) is solved for Δt to yield $\Delta t \ll 1 \text{ ns}$. A simulation time step of a nanosecond or longer would not just limit spatial resolution, but would produce a simulation with the incorrect reaction rate. On the other hand, the use of a sufficiently short time step would make most simulations run much too slowly to be useful.

Next, we turn to the long time step limit, given by the condition $s \gg \sigma_b$. Now, any correlations between the positions of reactants are eliminated after the simulation executes one iteration of the diffusion algorithm, so the probability that a certain A will react with a certain B is just the ratio of the volume of a sphere of radius σ_b to the total system volume. Multiplying by the numbers of A and B molecules and changing to concentrations yields the numerical rate constant for the long time step limit:

$$k_{Ni} = \frac{4\pi}{3}\sigma_b^3 \Delta t, \quad \Delta t \rightarrow \infty. \quad (20)$$

Using the same reaction rate and diffusion coefficients as above, this equation is not valid until the mutual rms step length is greater than around 100 nm (using $s = 10\sigma_b$). A step length this long precludes the possibility of attaining spatial resolution anywhere near the sizes of molecules, making it not generally useful either.

Between these limits, k_{Ni} cannot be solved analytically, so it was calculated numerically to create a look-up table for later use (available as supplementary information). The number of variables was minimized by dividing all lengths by the binding radius, leading to unitless variables: $k_{Ni}\Delta t/\sigma_b^3$ is the reduced reaction rate, s'/σ_b is the reduced rms step length, and $\sigma_b/\sigma_b = 1$ is the reduced binding radius. To perform the calculation, a tabulated RDF (500 equally spaced data points, with reduced radii from 0 to 10) was evolved over time exactly as it would evolve in the simulation algorithm, by alternating

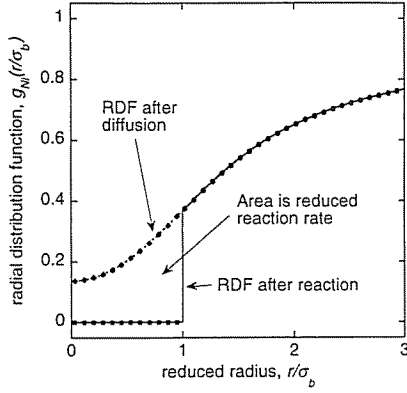


Figure 5. Method used for calculating the reduced bimolecular reaction rate, $k_{Ni} \Delta t / \sigma_b^3$, for irreversible reactions. A tabulated RDF was alternately integrated with Green's function to simulate diffusion and set to 0 between $r = 0$ and $r = 1$ to simulate reactions. After steady-state was reached, the RDF after diffusion (diamonds and dashed line) and the RDF after absorption (squares and solid line) were saved and the area between $r = 0$ and $r = 1$ of the former function was integrated to find the reduced reaction rate. Tabulated RDFs for irreversible reactions extended to a reduced radius of 10, while those for irreversible reactions extended to $\sigma_b' + 3$; all RDFs used 500 data points (for clarity, only every fifth data point is shown).

diffusion steps and irreversible reaction steps. The calculation began with either the RDF in equation (16) or with $g(r) = 1$ for all $r > 1$ and was continued until the RDF converged to a steady-state result (figure 5).

Conceptually, diffusion of an RDF from an initial state to its state after time Δt is computed by convolving the three-dimensional radial distribution function with a three-dimensional Gaussian with standard deviation s' (analogous to equation (4)). Because of rotational symmetry, this convolution simplifies to the integral of the product of the RDF and the appropriate Green's function [14, 29], given as $gm(r, r', s)$:

$$g_{Ni, \text{final}}(r) = \int_0^\infty 4\pi r'^2 gm(r, r', s) g_{Ni, \text{initial}}(r') dr' \quad (21)$$

$$gm(r, r', s) = \frac{1}{4\pi r r'} [G_s(r - r') - G_s(r + r')]. \quad (22)$$

Most of the integral in equation (21) was calculated numerically using the tabulated RDF and the trapezoid method [35]. The rest of the integral, from the end of the tabulated RDF to infinity, was calculated by extrapolating the RDF with a function of the form $1 + a/r$ which is the general solution of equation (3) with the boundary condition that $g_{Ni}(r)$ tends to 1 for large r ; a is a fitting parameter that was found using the final 10% of the tabulated RDF. The analytic integral for the extrapolated portion, which was then combined with the numerical integral, is

$$\begin{aligned} & \int_{r_1}^\infty 4\pi r'^2 gm(r, r', s) \left(1 + \frac{a}{r'}\right) dr' \\ &= 4\pi s^2 r_1 gm(r, r_1, s) + \frac{1}{2}(e_- + e_+) + \frac{a}{2r}(e_- - e_+) \quad (23) \end{aligned}$$

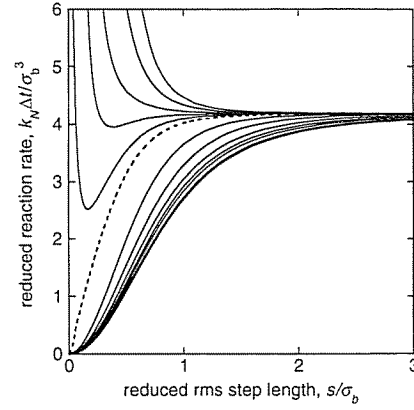


Figure 6. The reaction rate for the numerical algorithm as a function of the algorithm parameters, which are the rms step length and binding and unbinding radii. The bold line (lowest line) represents irreversible reactions. From top to bottom, the other lines are for reversible reactions with reduced unbinding radii that are 0, 0.5, 0.7, 0.8, 0.9, 1.0 (dashed line), 1.6, 2.5, 4.0, 6.3 and 10.0. Shown are interpolations and extrapolations from tabulated data, extended with analytical solutions where available.

$$e_\pm \equiv \operatorname{erfc} \frac{r_1 \pm r}{s\sqrt{2}}. \quad (24)$$

After a diffusion step, the reduced reaction rate was computed by numerically integrating the tabulated RDF from 0 to the reduced binding radius (figure 5):

$$\frac{k_{Ni} \Delta t}{\sigma_b^3} = \int_0^1 4\pi r^2 g_{Ni}(r) dr. \quad (25)$$

Afterwards, these values of $g_{Ni}(r)$ were set to 0 to mimic the reaction portion of the simulation algorithm. The RDF was considered to have achieved steady-state when the reduced rate constant varied by less than 1 part in 10^5 over sequential iterations (figure 4(C)).

To improve accuracy and provide an error estimate, the calculation was run in two directions: starting with long rms step lengths, leading to reduced rate constants that decreased asymptotically as steady-state was approached, and vice versa. These results were averaged to yield best estimates for the reduced rate constants. The difference between results was never greater than 5%, implying that calculation errors due to the RDF not being at steady-state are likely to be less than 2.5%. Other potential errors were minimized by increasing the density of data points and the maximum tabulated radius until changes in results were much less than the errors quoted above. Also, it was confirmed that the RDF approached equation (16) for short time steps and a step function for long time steps.

The result of these calculations is the bold line at the bottom of figure 6, produced with a smooth interpolation of the calculated rates. Although the figure is shown with reduced units, this line represents k_{Ni} as a function of σ_b and Δt , making it the equivalent of equation (19), but for the numerical algorithm. The ends of the curve conform to

the limits in equations (19) and (20), which are rewritten in reduced form:

$$\frac{k_{Ni} \Delta t}{\sigma_b^3} = 2\pi s^2, \quad \Delta t \rightarrow 0 \quad (26)$$

$$\frac{k_N \Delta t}{\sigma_b^3} = \frac{4\pi}{3}, \quad \Delta t \rightarrow \infty. \quad (27)$$

Thus, we have solved the forward problem, which is the solution of the rate constant that is actually simulated in terms of the simulation parameters. Since what is needed is a solution to the inverse problem, which is the binding radius that the simulation needs to use in order to reproduce a known reaction rate, an iterative search routine was written to invert the interpolated function. Using our *Smoldyn* program, we verified that irreversible bimolecular reaction rates are accurately simulated using a wide range of time steps.

4.3. Reversible reactions

The reversible reaction $A + B \leftrightarrow C$ has the additional complication of geminate recombinations. This topic is addressed on a general level before we derive reversible reaction rates for the Smoluchowski model and the numerical algorithm.

The probability of a geminate recombination is denoted by ϕ . Of all the forward reactions that occur when the system is at equilibrium, which occur with reaction rate k_r , a fraction $1 - \phi$ are non-geminate reactions. This portion of the reactants does not share a common history so all of their dynamics, including the rate at which they react (k_i), are completely equivalent to the irreversible situation considered previously. This leads to a general relationship between the irreversible and reversible rate constants at equilibrium (true for the model, simulations and all physical systems):

$$k_i = (1 - \phi)k_r. \quad (28)$$

We are not suggesting that k_r is larger than k_i because of the physically unreasonable idea that reaction reversibility somehow makes molecules more reactive. Instead, if a reaction is reversible, the reactants are generated in close proximity to each other by the back reaction, which leads to faster reactant encounters and a higher reaction rate. The correct value for 'the forward reaction rate constant' depends on the conditions under which it was measured. If the experimental system was at equilibrium, then there must have been geminate reactions as well as non-geminate reactions, leading to the measurement of the larger reaction rate constant, k_r . On the other hand, if the product was removed as fast as it was formed, then there were no geminate reactions, leading to the measurement of the smaller irreversible rate constant, k_i . Below, we derive results for the equilibrium situation.

4.4. Reversible reactions, Smoluchowski model

At equilibrium, the same number of A and B molecules are produced in back reactions as are lost in forward reactions, implying that the source of B molecules at σ_u exactly matches the sink at σ_b . This implies that there is no net flux of B towards

A molecules outside a distance σ_u and, to be consistent with zero flux and the boundary condition that $g(\infty) = 1$, the RDF must equal 1 for all $r > \sigma_u$. Equation (3) was solved using this modified boundary condition to yield the RDF for the Smoluchowski model for reversible reactions (figure 4(B)):

$$g_{Sr}(r) = 1 - \frac{\sigma_b(\sigma_u - r)}{r(\sigma_u - \sigma_b)}, \quad \sigma_b < r < \sigma_u. \quad (29)$$

As before, equation (17) yields the equilibrium rate constant. Combing the result with equation (28) yields the reversible reaction rate and the probability of geminate recombination:

$$k_{Sr} = \frac{k_{Si}}{1 - \phi_S} \quad (30)$$

$$\phi_S = \frac{\sigma_b}{\sigma_u}. \quad (31)$$

The latter result [12] confirms the statement made earlier that geminate rebinding in the model system becomes certain as σ_u is decreased to σ_b . It also has the intuitively reasonable property that ϕ_S decreases to zero as σ_u is increased to infinity.

4.5. Reversible reactions, numerical algorithm

The reaction rate for simulated reversible reactions was computed numerically in nearly the same manner as for irreversible reactions, although now for a series of σ'_u values, where $\sigma'_u = \sigma_u/\sigma_b$. While the unbinding radius cannot be less than the binding radius in the model system, there is no such restriction for the numerical algorithm, so these reduced reaction rates were computed as well. Back reactions were included in the rate computation by evaluating the flux of the RDF into the reduced binding radius with equation (25), and transferring it to the RDF at the reduced unbinding radius (figure 4(D)). Conceptually, this transferred flux forms a Dirac delta function at σ'_u after a reaction step. To improve numerical accuracy, the delta function was diffused separately and then added to the RDF one step later; a diffused delta function is simply $\text{grn}(r, \sigma_u, s)$. The reduced reaction rates are shown with light lines in figure 6. They represent k_{Nr} as functions of σ_b , σ_u and s , making them the numerical algorithm equivalent of equation (30). Using an iterative search routine, the function was inverted to solve for the simulation parameters σ_b and σ_u from the experimentally known values k_r and ϕ .

Errors in these data are estimated to be less than 2.1%. The numerical RDFs approached the analytical RDF in equation (29) for short time steps and the ends of the curves in figure 6 approach the limits found with equations (27) and (30).

4.6. Bimolecular reactions with identical reactants

A final subtle point concerns the calculation of simulation parameters for reactions with the form $A + A \rightarrow C$. Using the methods given above, the simulated reaction rate turns out to be half as large as expected. The reason is that there are $n_A n_B$ possible distinct collisions for the reaction $A + B \rightarrow C$, whereas there are only $n_A(n_A - 1)/2$ distinct A-A collisions

for $A + A \rightarrow C$ [36], where n_A and n_B are the total numbers of A and B molecules. Assuming the experimental reaction rate was measured with many reactant molecules, the factor $n_A - 1$ simplifies to just n_A , leading to the factor of 2 of over-counting. The easiest correction method is to simply double all experimental rate constants for reactions with identical reactants before calculating simulation parameters.

5. Analysis of simulated dynamics

Using the binding and unbinding radii derived above, reaction rates with the bimolecular reaction algorithm will match experimentally determined reaction rates for any system at steady-state and using any length simulation time step. If the geminate recombination probabilities are known or can be guessed, simulation results will agree with them as well. However, away from steady-state, reaction rates differ slightly between reality and the model (the model treats all reactions as though they are diffusion limited) and between the model and the simulation. These issues are investigated here. It is shown that the errors frequently offset each other such that simulation results are actually closer to reality than the model is. We also find a way to estimate the geminate recombination probability from the reaction activation energy.

As seen in figure 4, the numerical RDF is discontinuous at the binding radius, unlike the model result, but suggestive of the RDF for the Collins and Kimball model [14, 17, 37]. This differs from the Smoluchowski model in that a reaction does not always occur when reactants collide, but occurs at a maximum reaction rate, as would arise from an activation barrier at the binding radius. To accomplish this, the statement that $g_S(r) = 0$ at $r = \sigma_b$ is replaced with the condition [29]:

$$\left. \frac{\partial g_C(r)}{\partial r} \right|_{\sigma_b} = \frac{g_C(\sigma_b)}{\gamma}. \quad (32)$$

The new subscript 'C' is used for the Collins and Kimball model; to be rigorous, both sides of the equation are evaluated at the limit of $r \rightarrow \sigma_b^+$. As mentioned previously, the physical picture is complicated because each A-B pair that collides once will almost certainly collide an infinite number of times, implying that the reaction probability at each individual collision is infinitesimal. Despite this, equation (3) can be solved with the new boundary condition to yield the steady-state RDF (figures 4(E) and (F)), the reaction rate constant for irreversible [14] and reversible reactions, and the probability of geminate recombination for reversible reactions:

$$g_{Ci}(r) = 1 - \frac{\sigma_b^2}{r(\sigma_b + \gamma)}, \quad r > \sigma_b \quad (33)$$

$$k_{Ci} = \frac{4\pi\sigma_b^2 D}{\sigma_b + \gamma} \quad (34)$$

$$g_{Cr}(r) = 1 - \frac{\sigma_b^2(\sigma_u - r)}{r(\sigma_u\gamma + \sigma_b\sigma_u - \sigma_b^2)}, \quad \sigma_b < r < \sigma_u \quad (35)$$

$$k_{Cr} = \frac{4\pi\sigma_b^2\sigma_u D}{\sigma_u\gamma + \sigma_b\sigma_u - \sigma_b^2} \quad (36)$$

$$\phi_C = \frac{\sigma_b^2}{\sigma_u(\sigma_b + \gamma)}. \quad (37)$$

The RDFs for the numerical algorithm are seen to be similar to those of the Collins and Kimball model (figure 4).

Suppose the reactants are maintained in a well-mixed state. This removes all diffusion effects from the reaction rate, making it limited only by the activation energy. In the Smoluchowski model, the discontinuity of this well-mixed RDF at σ_b implies an infinite slope at σ_b and an infinite reaction rate (using equation (17)). In contrast, the boundary condition of the Collins and Kimball model enforces a slope of $1/\gamma$ at σ_b and hence the *activation-limited* rate constant for the Collins and Kimball model,

$$k_{Ca} = 4\pi\sigma_b^2 D \gamma^{-1}. \quad (38)$$

This rate constant is also called the intrinsic rate constant [37], with the loose interpretation that it is the reaction rate for a pair of molecules that are already in contact. Equations (36) and (38) are simplified to highlight the relationship between the Smoluchowski and Collins and Kimball models:

$$k_{Ci}^{-1} = k_{Si}^{-1} + k_{Ca}^{-1} \quad (39)$$

$$k_{Cr}^{-1} = k_{Sr}^{-1} + k_{Ca}^{-1}. \quad (40)$$

Along with the rest of the Collins and Kimball model, these reaction rates vary smoothly between the Smoluchowski description when $\gamma \rightarrow 0$ and $k_{Ca} \rightarrow \infty$, to a well-mixed system when $\gamma \rightarrow \infty$ and $k_{Ca} \rightarrow 0$. The Collins and Kimball model is a significant improvement to the Smoluchowski model because it can capture a whole range of reaction types, from diffusion limited to activation limited, while remaining fundamentally simple.

An analogous activation-limited rate constant is calculated for the numerical algorithm. A well-mixed RDF is diffused over one simulation time step with equation (21) and the reaction rate is found with equation (25) to yield

$$\begin{aligned} \frac{k_{Na}\Delta t}{\sigma_b^3} &= \frac{4\pi}{3} \left(\operatorname{erfc} \frac{\sqrt{2}}{s'} + s' \sqrt{\frac{2}{\pi}} \right) \\ &+ \frac{2\sqrt{2\pi}}{3} s' (s'^2 - 1) (e^{-2/s'^2} - 1). \end{aligned} \quad (41)$$

This result approaches infinity as Δt is reduced to zero and the simulation approaches the Smoluchowski model, while it becomes rate limiting with long time steps. Thus, Δt is a parameter in the numerical algorithm that adjusts the simulated dynamics from diffusion limited to activation limited, much as γ is a tunable parameter in the Collins and Kimball model.

The probabilities of geminate recombination form yet another similarity. From equation (37) and the model constraint that $\sigma_u \geq \sigma_b$, ϕ_C can decrease towards zero but cannot exceed $\sigma_b/(\sigma_b + \gamma)$. Similarly, ϕ_N can be made arbitrarily small by using a large unbinding radius but it has a maximum value because the simulation σ_u cannot be decreased below zero. As with the activation-limited rate constants, the maximum ϕ values depend on γ for the Collins and Kimball model and Δt for the numerical algorithm.

The upper limit on ϕ_C can be used to address an issue that has been largely ignored up to this point: how is one supposed to choose the unbinding radius for a simulation? Using equation (28) and the curves in figure 6, it is possible to calculate the simulation parameters σ_b and σ_u from experimentally measured k_r and ϕ values, provided that geminate recombination data can be found. Unfortunately, these data are nearly non-existent. A solution comes from the Collins and Kimball model in which it is physically most reasonable to set σ_u equal to σ_b and to limit the rate of geminate reactions with an activation barrier:

$$\phi_C = \frac{k_{Ca}}{k_{Ca} + k_{Si}}, \quad \sigma_u = \sigma_b. \quad (42)$$

The ‘C’ subscripts are retained here because the equation is only strictly accurate with the approximations of the Collins and Kimball model. However, the model is often a good description of physical systems, so the relationship is also likely to be reasonably accurate experimentally. If the activation-limited rate constant can be estimated, equation (42) yields ϕ , which can then be used to find σ_u for a simulation.

Recall that a simulation can be interpreted as periodic observations of a virtual system that evolves continuously. Also, an exact bimolecular reaction algorithm would use the binding radius from the Smoluchowski model and would consider a reaction as having occurred between a pair of molecules if they had come closer than σ_b during a time step. Analogous exact algorithms can be imagined for the Collins and Kimball model or for any of several further improvements to these classic models [18, 34, 38, 39]. While the simulation does not reproduce any of them exactly, similarities with the Collins and Kimball model include the profile of the RDF, the activation energy and the geminate recombination probability. This suggests that the simulated dynamics, whether at steady-state or not, are likely to be reasonably consistent with the behavior that would be observed with the Collins and Kimball model. Of course, the simulation time step applies to every reaction in a simulated reaction network, so one cannot independently control the dynamics of multiple reactions. However, this is unlikely to have practical consequences because differences between steady-state and non-steady-state reaction rates are so small that they are very difficult to measure experimentally [32, 40].

6. Examples

6.1. Irreversible reaction

Our first example demonstrates that the algorithms can accurately simulate bimolecular reactions at and away from steady-state, using either diffusion-limited or activation-limited dynamics. It is based on a recent experiment on the kinetics of an acid–base reaction [32]. Starting with well-mixed acid (AH) and base (B) molecules, the experiment was initiated by photo-exciting the acid with a fast laser pulse. An irreversible proton transfer occurred when an excited acid molecule contacted a base molecule, with the reaction $AH + B \rightarrow A + BH$. Using transient fluorescence measurements

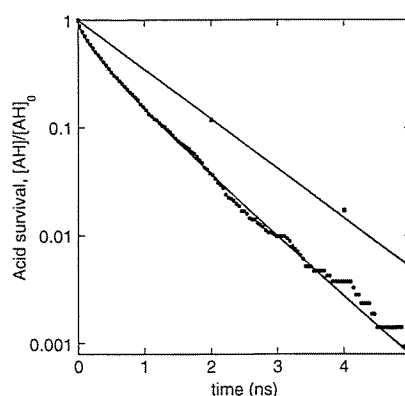


Figure 7. Progress of a bimolecular acid–base reaction that starts as a well-mixed system and approaches steady-state. The lower line is the non-exponential Smoluchowski solution for diffusion-limited dynamics (equation (43)) and the nearby solid circles are from a diffusion-limited simulation. Parameters: $D_{AH} = 10^{-3} \text{ cm}^2 \text{ s}^{-1}$, $D_B = 0$, volume = 10^6 nm^3 , $[AH]_0 = 3.3 \times 10^{-3} \text{ M}$ (2000 molecules), $[B]_0 = 0.2 \text{ M}$ (120000 molecules), $k_i = 5.3 \times 10^9 \text{ M}^{-1} \text{ s}^{-1}$, $k_u = 5.1 \times 10^{10} \text{ M}^{-1} \text{ s}^{-1}$, $\sigma_b = 0.73 \text{ nm}$, $s = 0.063 \text{ nm}$, and $\Delta t = 0.002 \text{ ns}$ (only every 20th point is shown for clarity); runtime was 12 min on a Macintosh G4 laptop. The upper line is the exponential solution for activation-limited reactions (equation (44)) and the nearby solid squares are from a more nearly activation-limited simulation. Parameters are the same as before except $k_u = 6.5 \times 10^9 \text{ M}^{-1} \text{ s}^{-2}$, $\sigma_b = 1.81 \text{ nm}$, $s = 2.0 \text{ nm}$, and $\Delta t = 2 \text{ ns}$; runtime was 4 s.

of the acid, the authors showed that the reaction progress was in close agreement with Smoluchowski dynamics (they included the Debye–Hückel corrections that are required for ionic species, although these had minimal effect due to high salt concentrations). Using similar parameters as those in the experiment, the lower line in figure 7 represents the analytically derivable Smoluchowski result [14]:

$$[AH] = [AH]_0 \exp \left[-4\pi\sigma_b D[B]_0 \left(1 + \frac{2\sigma_b}{\sqrt{\pi Dt}} \right) t \right]. \quad (43)$$

The curve has a very steep slope initially because the reactants start well-mixed; then, it flattens out to a straight line on the log-linear coordinates, as the system approaches steady-state. Using the same diffusion coefficients and steady-state reaction rate, the reaction was simulated with a very short time step to make the simulated dynamics diffusion limited. Agreement between theory and simulation is seen to be excellent at all times, although stochastic effects become apparent when there are few molecules.

The upper curve in figure 7 represents the theoretical behavior for an activation-limited reaction, using the same steady-state rate constant as before:

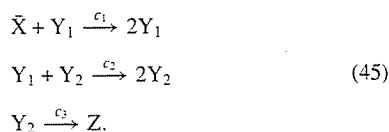
$$[AH] = [AH]_0 \exp(-k[B]_0 t). \quad (44)$$

Using a long time step, the same simulation algorithm accurately reproduced these activation-limited reaction dynamics as well.

Note that there are no adjustable parameters in either comparison. While it might be desirable to lower the time resolution of the former simulation and raise it for the latter one, this is impossible, because the length of the time step determines whether simulated dynamics are diffusion or activation limited. The diffusion-limited results satisfy the stated goal, which was that the observable simulation dynamics be as close as possible to the analytically derivable dynamics of the model system, while the activation-limited dynamics go an additional step, showing that it is also possible to simulate reactions that are not described by the Smoluchowski model.

6.2. Lotka–Volterra system

To demonstrate the value of stochastic spatial simulations, we turn to the canonical Lotka–Volterra system, which is a simple scheme that yields interesting dynamics. The reactions are [36]



The bar over the X indicates that its concentration is held constant. The system was introduced independently by Lotka and Volterra as ecological models [41]: Y_1 is a prey species that multiplies after feeding on X , and Y_2 is a predator species that multiplies after feeding on the prey Y_1 . Analysis reveals stable oscillations in the concentrations of Y_1 and Y_2 as well as a neutrally stable stationary solution:

$$Y_1 = \frac{c_3}{c_2} \quad Y_2 = \frac{c_1 X}{c_2}. \quad (46)$$

Using a simulation method that accounts for stochastic effects but not space, Gillespie showed that the stochastic behavior of these reactions is quite different from deterministic results [36]. In particular, the system does not remain at the stationary point, but develops regular oscillations with a widely varying amplitude (dashed lines in figure 8(A)).

These reactions were simulated with the algorithms presented here using the same rate constants and initial condition, and with the Y_1 and Y_2 molecules distributed randomly initially. Rather than including X molecules explicitly, the first reaction was simulated as a unimolecular reaction with a rate constant $c_1 X = 10$. Spontaneous pattern formation emerged just after the simulation began, one snapshot of which is shown in figure 8(B). This led to dynamics that are markedly different from those found with either deterministic results or the Gillespie algorithm. In the spatial simulation, the oscillations are less regular, transitions are sharper, and there are occasional extreme deviations away from the steady-state solution. Many of these behaviors have been seen before, although most prior results used continuously variable reactant concentrations and/or a discrete spatial lattice [42–44]. Thus, with each level of detail that is added to a simulation, including first stochastics and then space, there can be large effects on the resulting dynamics of the system as a whole.

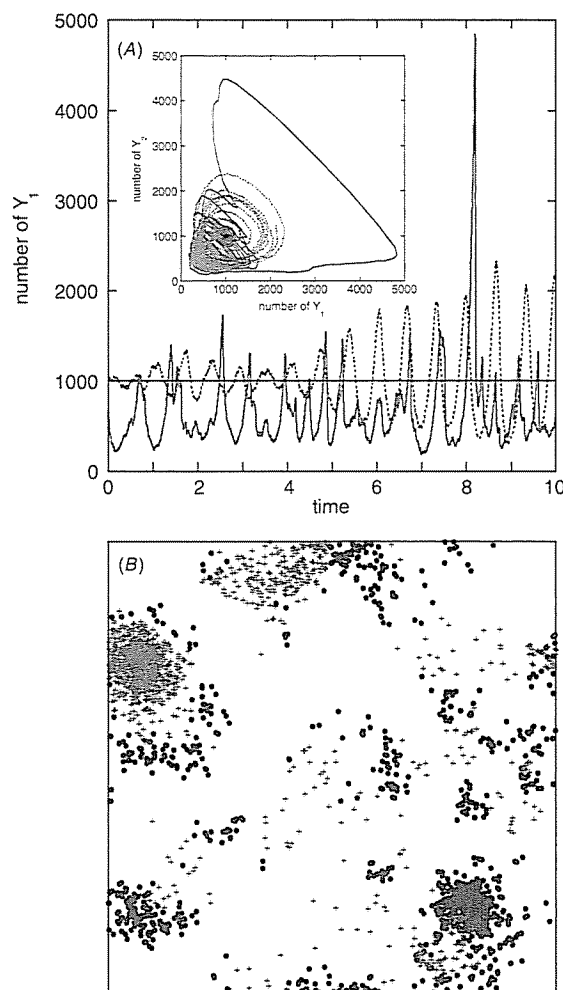


Figure 8. Dynamics of a Lotka–Volterra system. (A) Time course of the number of Y_1 molecules shown with three different models. The black line at $Y_1 = 1000$ is the deterministic solution for the neutrally stable stationary point; the green dashed line, created with the Gillespie algorithm, includes stochasticity but no spatial information; the red solid line, created with the algorithms presented here, includes both stochasticity and spatial detail. Note that the behaviors are quite different for the three models, demonstrating the value of the higher level of detail. Inset: a phase space portrait of the data shown in the time series using the same line styles; the deterministic solution is a point at $Y_1 = Y_2 = 1000$. (B) A snapshot of the spatial simulation shown in the previous panels, with blue dots for Y_1 molecules and green '+' symbols for Y_2 . This image was taken at time 2.6, which was during a sharp decline of Y_1 and a growth of Y_2 , where most of this activity is occurring in the upper left corner of the image. The high degree of pattern formation emerged spontaneously from a nearly homogeneous initial state and was very transient. Reaction parameters: $X = 10^5$, $c_1 = 0.0001$, $c_2 = 0.01$, $c_3 = 10$, and initial values are $Y_1 = Y_2 = 1000$. Simulation parameters: volume dimensions are 200 on x and y , and 20 on z , with periodic boundaries, 10 units of time were simulated in steps of 0.001 time units, and diffusion constants are 100 for each Y_1 and Y_2 , leading to rms step lengths of 0.447. The $Y_1 + Y_2$ reaction was simulated with $\sigma_b = 3.55$. Runtime was 70 s.

7. Conclusions and outlook

The algorithms presented here allow the accurate simulation of reaction networks with the inclusion of the stochasticity that arises from the discreteness of molecules and with spatial detail that can be accurate down to near the size scale of individual molecules. Simulation algorithms for diffusion, surface interactions and zeroth- and first-order reactions could be made exact, meaning that simulation results were shown to match the analytical results of an idealized model system using any length simulation time step. However, long time steps lead to discrepancies when different processes are coupled together. Bimolecular reactions were made as efficient as possible using the rule that two molecules react whenever they are found to be within their binding radius at the end of a time step. This parameter is calculated from the steady-state reaction rate constant and the simulation time step using the data in figure 6, yielding reaction rates that are exact when the system is at steady-state and are reasonably accurate at other times. The simulated reaction dynamics are similar to those of a Collins and Kimball type model and, likewise, can be characterized as diffusion or activation limited.

The examples demonstrate that these simulation algorithms work well in practice. Bimolecular reaction rates are simulated accurately at and away from steady-state with either activation- or diffusion-limited dynamics. Various levels of simulation detail with the Lotka–Volterra reactions demonstrate that the overall dynamics of a system of coupled reactions can be sensitive to stochastic and spatial effects. The algorithms run quickly enough that these examples were simulated on a laptop computer in several minutes.

These algorithms open up new avenues of research, allowing simulation detail at a level that was previously unattainable. They fill a gap between the more accurate and very computationally intensive molecular dynamics calculations, and the much coarser differential equation based reaction–diffusion methods. They are likely to be most useful for systems with several thousand molecules and with complex spatial constraints. For example, our *Smoldyn* program is currently being used to examine the diffusion and reaction of signaling molecules in the *E. coli* chemotaxis pathway, including effects from intracellular macromolecular crowding [23]. We also used these methods to investigate the repeated bindings of a single ligand to a cluster of receptors [24].

An additional algorithm that would be useful is one for simulations of molecule–fiber interactions, because that would allow studies of polymer growth, microtubule dynamics, DNA transcription and RNA translation, to name but a few examples. With this addition, and perhaps a few others, it should be possible to simulate essentially any biochemical process using individual molecules and a high level of spatial resolution. At that point, the hurdles to simulating an entire bacterium are computational power and experimentally determined inputs for the simulation.

Supporting information. Implementation of the bimolecular reaction algorithm presented here requires a look-up table for the data shown in figure 6. These data are available via the Internet at the *Physical Biology* website at <http://www.iop.org/EJ/journal/physbio>. They are presented in tabular form and in the code of several C language routines. The routines

execute data interpolation, extrapolation and tabular inversion so as to yield simulation parameters from experimental values. The C code that was used to generate the data table is included as well. The *Smoldyn* executable program, source code, and sample input files are available at the author's website: <http://sahara.lbl.gov/~sandrews/software.html>.

Acknowledgments

This work was funded by NIGMS grant GM64713, the Genomes to Life Project of the US Department of Energy, and by an NSF postdoctoral fellowship in biological informatics awarded to SSA. Comments on the manuscript by Dan Gillespie and Tom Shimizu are appreciated, as is assistance from Adam Arkin.

Appendix. Implementation details

A.1. Diffusion

In the diffusion algorithm, a uniformly distributed random number is converted to a normally distributed number for each spatial dimension, for each molecule, and at every time step. The Box–Muller transformation [35] is easy to implement but the required trigonometric calculations make this heavily used algorithm run slowly. Instead, the use of a look-up table is nearly as accurate and runs much faster. To create an n element look-up table, indexed from 0 to $n - 1$, the i th element is

$$X_i = \sqrt{2} \operatorname{erf}^{-1} \left(\frac{2i + 1}{n} - 1 \right). \quad (\text{A1})$$

If i is a random integer between 0 and $n - 1$, X_i is a normally distributed random variable with standard deviation 1, and σX_i is the desired normal deviate with mean 0 and standard deviation σ . This equation is derived by integrating a Gaussian probability density with unit variance to yield an error function and then inverting the result [35]. A table is not quite as accurate as an analytical transformation because there are typically fewer table entries than available random numbers although this is not a significant constraint for Brownian dynamics because the number of possible displacements for each molecule is the cube of the number of table entries for a three-dimensional system with one time step, and increases exponentially with additional time steps.

A.2. Surface interactions

Surface interactions are sufficiently easy to simulate that they are described in the main text. The one exception is that spatial partitions, described below, can be used to minimize the number of molecule–surface interactions that need to be checked.

A.3. Zeroth-order reactions

During one time step, the probability that exactly j molecules of type A are produced is given with a Poisson distribution [28]:

$$\operatorname{Prob}(j) = \frac{(k_0 \Delta t)^j \exp(-k_0 \Delta t)}{j!}. \quad (\text{A2})$$

This can be computed easily with a rejection method [35]. Some computational efficiency can be gained by calculating the required probabilities during program initialization and storing them in look-up tables (one for each zeroth-order reaction). However, the overall improvement in speed is typically negligible because only one Poisson deviate is required for each zeroth-order reaction at each time step.

A.4. Unimolecular reactions

Rather than re-calculating the reaction probabilities given in equation (14) at each time step, it is faster to calculate them just once for each possible unimolecular reaction during program initialization. Additional computational efficiency is gained by summing these probabilities. Using i as an index for a pathway by which a molecule can undergo a unimolecular reaction, the reaction probabilities for pathway 1 to i are summed to form a list of cumulative reaction probabilities. At each time step during the simulation, a specific molecule reacts by pathway i if a uniform deviate is less than the i th stored cumulative probability value and greater than the preceding value.

A.5. Bimolecular reactions

Although it complicates the implementation, spatially partitioning the simulation volume [10, 45] is essential to reduce the proportionality of the runtime for bimolecular reactions from second order in the total number of molecules to first order. To do this, the program maintains a separate list of the molecules for each region. When checking for bimolecular reactions, the program only needs to investigate pairs of molecules that are in the same or neighboring regions. In the same way, partitions also speed up the simulation of surface interactions.

A.6. Simulation time step

Discrepancies between the simulated dynamics and those of the model system arise from the following: spatial resolution that cannot exceed the rms step length (figure 1), bimolecular reaction dynamics that are closer to the Collins and Kimball model than the Smoluchowski model, and the coupling of molecular processes. The last error is very difficult to analyze, so we present a practical rule-of-thumb instead. A simulation is run with a trial time step that is short enough to yield the needed spatial resolution and again with a time step that is half as long. The longer time step is short enough if the results between the two runs are essentially the same (recalling that they will always differ somewhat due to stochasticity); otherwise, the time step needs to be reduced. This works because all errors decrease monotonically with smaller simulation time steps.

Glossary

Activation limited. Chemical reactions in which the reaction rate is fully determined by an activation energy barrier, making the reactant diffusion coefficients unimportant.

Binding radius. The separation at which a pair of reactant molecules react.

Brownian dynamics. A simulation method for molecular diffusion in which each molecule takes a step chosen from a Gaussian distribution, at each time step.

Brownian motion. Diffusive motion of a molecule that has been idealized to obey Fick's laws at all size and time scales, leading to an infinitely detailed trajectory.

Collins and Kimball model. An extension of the Smoluchowski model that includes an activation energy barrier for bimolecular reactions.

Diffusion influenced. Chemical reactions in which reactant diffusion is slow enough to influence the reaction rate.

Diffusion limited. Chemical reactions in which reactant diffusion is so slow that it completely determines the reaction rate.

Geminate recombination. The reaction of a pair of product molecules that were created from the same reactant molecule, back to yield a reactant.

Mutual diffusion coefficient. The sum of the diffusion coefficients for two reactants.

Mutual rms step length. The rms step length that is calculated from a mutual diffusion coefficient.

Radial distribution function (RDF). The distribution of distances between individual molecules of one type and those of another type, averaged over every pair of molecules.

Root mean square (rms) step length. The average length of a step for a molecule in a Brownian dynamics simulation.

Smoldyn. A general purpose stochastic spatial simulation program that incorporates all the algorithms described here.

Smoluchowski model. An analytical model of chemical reactions in which spherical molecules react upon collision.

Steady-state. A situation in which neither the spatial correlation of reactants nor the bimolecular reaction rate constant changes over time.

Unbinding radius. The initial separation between a pair of products of a reversible reaction, introduced to reduce the probability of back reactions.

Well mixed. A situation in which reactant molecules are mixed uniformly throughout the simulation volume; the only spatial correlation is that reactants do not overlap each other.

References

- [1] Arkin A P 2001 *Curr. Opin. Biotechnol.* **12** 638
- [2] Slepchenko B M, Schaff J C, Carson J H and Loew L M 2002 *Annu. Rev. Biophys. Biomol. Struct.* **31** 423
- [3] Takahashi K *et al* 2002 *IEEE Intell. Syst.* **17** 64
- [4] Barkai N and Leibler S 1997 *Nature* **387** 913

- [5] Levin M D, Morton-Firth C J, Abouhamad W N, Bourret R B and Bray D 1998 *Biophys. J.* **74** 175
- [6] Duke T A J, LeNovère N and Bray D 2001 *J. Mol. Biol.* **308** 541
- [7] Ryan K R and Shapiro L 2003 *Annu. Rev. Biochem.* **72** 367
- [8] Kholodenko B N, Brown G C and Hoek J B 2000 *Biochem. J.* **350** 901
- [9] Rao C V, Wolf D M and Arkin A P 2002 *Nature* **420** 231
- [10] Stiles J R and Bartol T M 2001 Monte Carlo methods for simulating realistic synaptic microphysiology using MCell *Computational Neuroscience: Realistic Modeling for Experimentalists* ed E De Schutter (Boca Raton, FL: CRC Press)
- [11] von Smoluchowski M V 1917 *Z. Phys. Chem.* **92** 129
- [12] Berg H C 1993 *Random Walks in Biology* 2nd edn (Princeton, NJ: Princeton University Press)
- [13] Elowitz M B, Surette M G, Wolf P-E, Stock J B and Leibler S 1999 *J. Bacteriol.* **181** 197
- [14] Rice S A 1985 *Diffusion Limited Reactions (Comprehensive Chemical Kinetics vol 25)* ed C H Bamford, C F H Tipper and R G Compton (Amsterdam: Elsevier)
- [15] Schnell S and Turner T E 2004 *Prog. Biophys. Mol. Biol.* **85** 235
- [16] Northrup S H and Erickson H P 1992 *Proc. Natl Acad. Sci. USA* **89** 3338
- [17] Collins F C and Kimball G E 1949 *J. Colloid Sci.* **4** 425
- [18] Agmon N 1984 *J. Chem. Phys.* **81** 2811
- [19] Berlin Y A, Cordier P and Delaire J A 1980 *J. Chem. Phys.* **73** 4619
- [20] Noyes R M 1955 *J. Am. Chem. Soc.* **77** 2042
- [21] Atkins P W 1986 *Physical Chemistry* 3rd edn (New York: Freeman)
- [22] Northrup S H and Hynes J T 1980 *J. Chem. Phys.* **73** 2700
- [23] Lipkow K, Andrews S S and Bray D 2004 *J. Bacteriol.* at press
- [24] Andrews S S and Bray D 2004 in preparation
- [25] Crank J 1975 *The Mathematics of Diffusion* 2nd edn (Oxford: Oxford University Press)
- [26] Edelman A L and Agmon N 1993 *J. Chem. Phys.* **99** 5396
- [27] Ermak D L and McCammon J A 1978 *J. Chem. Phys.* **69** 1352
- [28] Snell J L 1988 *Introduction to Probability* (New York: Random House)
- [29] Carslaw H S and Jaeger J C 1959 *Conduction of Heat in Solids* 2nd edn (Oxford: Clarendon)
- [30] Zon J S v and Wolde P R T 2004 Preprint q-bio. MN/0404002
- [31] Stundzia A B and Lumsden C J 1996 *J. Comput. Phys.* **127** 196
- [32] Cohen B, Huppert D and Agmon N 2000 *J. Am. Chem. Soc.* **122** 9838
- [33] McQuarrie D A 2000 *Statistical Mechanics* (Sausalito, CA: University Science Books)
- [34] Szabo A 1989 *J. Phys. Chem.* **93** 6929
- [35] Press W H, Flannery B P, Teukolsky S A and Vetterling W T 1988 *Numerical Recipes in C. The Art of Scientific Computing* (Cambridge, UK: Cambridge University Press)
- [36] Gillespie D T 1977 *J. Phys. Chem.* **81** 2340
- [37] Hynes J T 1985 The theory of reactions in solution *Theory of Chemical Reaction Dynamics* ed M Baer (Boca Raton, FL: CRC Press)
- [38] Weaver D L 1980 *J. Chem. Phys.* **72** 3483
- [39] Popov A V and Agmon N 2001 *J. Chem. Phys.* **115** 8921
- [40] Sikorski M, Krystkowiak E and Steer R P 1998 *J. Photochem. Photobiol. A* **117** 1
- [41] Boyce W E and DiPrima R C 1992 *Elementary Differential Equations* 5th edn (New York: Wiley)
- [42] Vilar J M G and Solé R V 1998 *Phys. Rev. Lett.* **80** 4099
- [43] Spagnolo B and Barbera A L 2002 *Physica A* **315** 114
- [44] Satulovsky J E and Tomé T 1997 *J. Math. Biol.* **35** 344
- [45] Frenkel D and Smit B 2002 *Understanding Molecular Simulation: from Algorithms to Applications* 2nd edn (San Diego, CA: Academic)